International Journal of Heat and Fluid Flow 31 (2010) 154–171

Contents lists available at ScienceDirect

International Journal of Heat and Fluid Flow

journal homepage: www.elsevier.com/locate/ijhff

Numerical investigation of low Reynolds number flow past two and three circular cylinders using unstructured grid CFR scheme

Atal Bihari Harichandan, Arnab Roy *

Department of Aerospace Engineering, IIT, Kharagpur 721 302, India

ARTICLE INFO

Article history:
Received 20 March 2009
Received in revised form 14 January 2010
Accepted 20 January 2010
Available online 13 February 2010

Keywords:
Incompressible Navier–Stokes solver
Finite volume method
Unstructured triangular mesh
Circular cylinder
Side-by-side arrangement
Tandem arrangement

ABSTRACT

An incompressible unsteady viscous two-dimensional finite volume Navier–Stokes solver is developed using "consistent flux reconstruction" technique on a collocated unstructured mesh comprising of triangular cells. In this solver, the full Navier–Stokes equations have been solved numerically in the physical plane itself without using any transformation to the computational plane. The cell face centre velocities are reconstructed explicitly by solving the momentum equations on flux reconstruction control volumes defined judiciously around the respective cell face centres. This is followed by solution of the cell centre pressure field using a discrete Poisson equation developed from the reconstructed velocities and updating the cell centre velocities by using an explicit scheme. In the present investigation, the solver has been applied to unconfined flow past a single cylinder, two cylinders and three cylinders for Reynolds number (Re) = 100 and 200. To validate the numerical code the present results for single and two cylinder arrangements were compared with results available from literature and found to be agreeing well. For the two and three cylinder configurations flow has been computed for various gaps between cylinders and for both side-by-side and tandem arrangements. Different wake patterns like in-phase and anti-phase synchronized wake patterns, flip-flopping, deflected wake patterns and steady wake patterns are observed depending on the Reynolds number and the gap spacing.

1. Introduction

Study of unsteady viscous flow past single or array of circular cylinders is challenging because of its inherent complexity. Detailed study of such flow field is worthwhile because it finds numerous real-life and industrial applications. In many areas of engineering, circular cylinders form the basic component of structures and machinery for example, heat exchange tubes, cooling systems for nuclear power plants, offshore structures, cooling towers, transmission cables, etc. These structures are exposed to either air or water flow, and therefore they experience flow-induced vibration, which could lead to structural failure under severe conditions. To avoid these situations and to have better structural designs, it is necessary to understand the details of fluid–structure interactions. Another aspect of this problem is the enhanced convective heat transfer to or from the cylinder surface due to the flow unsteadiness and interference of neighbouring cylinders in applications where there is significant temperature difference between the fluid and the cylinder surface.

The difficulty in predicting flow around multi-cylinders is increased when two or more of these cylinders are placed in proximity to each other. This is because the dynamic interaction between the shed vortices, shear layers and Karman vortex streets appears in the wake of the cylinders. Consequently, the wake behaves quite differently from that of an isolated single circular cylinder. The exact form of the interaction is highly dependent on the Reynolds number of the flow and on the arrangement of the cylinders. The geometrical configuration of two or more circular cylinders can be categorized in general into side-by-side, tandem and staggered arrangements with respect to the direction of the free-stream flow. These configurations have been studied experimentally and numerically by several researchers in the past.

Finite volume method with unstructured grid is most suitable for handling complex flow fields including flow field around multiple cylinders. Usually some suitable cell face centre flux reconstruction procedure is devised which incorporates the effect of neighbouring cell centre velocities and pressures in a more consistent manner. This eliminates the numerical instabilities in course of calculation. Several such procedures have been proposed by researchers after use of collocated finite volume approach gained popularity in the recent decades. Rhie and Chow (1983), Choi et al. (1993), Deng et al. (1994), etc., are some of the pioneering works in this area. Roy and Bandyopadhyay (2006) developed a technique which uses explicit calculation for both cell face centre flux reconstruction and cell centre momentum equation updating, which has eliminated the tedious matrix inversion procedures proposed in many former schemes.

* Corresponding author. Tel.: +91 3222 283020; fax: +91 3222 255303.
E-mail address: arnab@aero.iitkgp.ernet.in (A. Roy).

0142-727X/$ - see front matter © 2010 Elsevier Inc. All rights reserved.
doi:10.1016/j.ijheatfluidflow.2010.01.007

Recently, there has been significant progress in the area of incompressible flow calculations with unstructured finite volume method. Many research works have been reported on flow past single and two cylinders. The flows around two circular cylinders in side-by-side and tandem arrangements were studied by many researchers (Slaouti and Stansby, 1992; Chang and Song, 1990; Stansby and Slaouti, 1981; Mittal et al., 1997; Farrant et al., 2001). They mainly focused on the variation of force coefficients for the two cylinders as well as the symmetric and asymmetric wake patterns developed in the downstream region of the cylinders. Jester and Kallinderis (2003) numerically investigated incompressible flow past a pair of cylinders arranged in tandem, side-by-side and staggered fashion at Re = 80 and 1000. They also experimentally observed flow physics such as hysteresis effects and bistable biased gas flow in tandem arrangements. Kang (2003) numerically investigated two-dimensional flow over two circular cylinders in a side-by-side arrangement at low Reynolds numbers using the immersed boundary (IB) method. A total of six kinds of wake patterns were observed from his simulations. He reported that the characteristics of flow significantly depend both on the Reynolds number and gap spacing, with the latter much stronger than the former. Mizusima and Ino (2008) investigated the stability and transition of flow past a pair of circular cylinders in a side-by-side arrangement by numerical simulation and linear stability analyses. They reported various flow patterns around the cylinders due to instability of the steady symmetric flow that is realized at small Reynolds number. Liu et al. (2007) also numerically investigated the flow past two side-by-side identical circular cylinders with the unstructured spectral element method. They observed a total of nine kinds of wake patterns for various gap spacing between the cylinders and the Reynolds number. Silva et al. (2007) presented a two-dimensional numerical solution of flows around different bluff bodies at Re = 100 and 200 using the IB method. Simulations were carried out for two circular cylinders of different diameter in tandem, two cylinders of the same diameter in tandem and in side-by-side arrangements. The configurations of seven cylinders in a V-arrangement are also simulated. They applied the IB method mainly to focus on flow dynamics and patterns. Meneghini et al. (2001) investigated the shedding of vortices and flow interference between two circular cylinders in tandem and side-by-side arrangements by using a fractional step method. The simulations were performed for a Reynolds number range varying from 100 to 200 and the flow was solved using finite element method. They observed that in tandem arrangement, the mean value of drag coefficient of the downstream cylinder changes from negative to positive value when the gap between two cylinder centres is greater than three times of the cylinder diameter.

In the present investigation the numerical method proposed originally by Roy and Bandyopadhyay (2006) to solve incompressible Navier–Stokes equations using a collocated structured grid has been extended and applied on an unstructured collocated triangular finite volume grid. A fully explicit scheme is adopted for the calculation of both cell face velocities and flow variables at the cell centres. For calculation of cell face velocities "consistent flux reconstruction" (CFR) technique has been formulated on unstructured grid which is based on solving the momentum equations at each cell face explicitly. The present CFR unstructured grid solver would be called as 'CFRUNS'. The flux reconstruction cell on the face of the control volume is placed centrally between the two cells which share that face. The reconstruction volumes are chosen judiciously so that computational effort is still reduced as compared to the original method. A discrete pressure-Poisson equation is obtained by substituting the reconstructed cell face velocity expressions in the discrete continuity equation. The pressure-Poisson equation is solved iteratively using Gauss–Siedel method. The reconstructed cell face flux is substituted in both continuity and momentum equations. For updating the flow variables at the cell centres, the momentum equations are solved in an explicit manner in contrast to implicit scheme of Deng et al. (1994). In this paper, numerical results are reported for the flow past two and three cylinders in side-by-side arrangement and three cylinders in tandem arrangement at Re = 100 and 200. For each arrangement, suitable gap between the cylinders is maintained. It is a well known fact that the wake behind two cylinders is highly influenced by the gap between the cylinders and there exists a so-called critical gap, which is used to classify the flow patterns behind the cylinders into several categories (Ding et al., 2007). Based on experimental observation, a range of flow regimes characterized by a critical gap has been found by Williamson (1985) and by Zdravkovich (1977). Williamson (1985) found three flow patterns for the side-by-side arrangement, i.e. $T < 2.2D$, $2.2D < T < 5D$, $T > 5D$, where T represents the transverse gap between the two cylinders and D the diameter of the cylinder. Zdravkovich (1977) reported three flow regimes for cylinders placed in tandem: $L < 1.2–1.8D$, $1.2–1.8D < L < 3.4–3.8D$ and $L > 4D$, where L represents the longitudinal gap between the two cylinders. As suggested by Zdravkovich (1977), the value of the critical gap depends on the Reynolds number and may vary within a certain range. In the present study, numerical simulations are performed over two cylinders with transverse gaps of 1.5D and 3D in side-by-side arrangement. The two-cylinder flow bears similarity to flow over more-than-two circular cylinders in many aspects such as synchronization and merging of wakes, deflection and flip-flopping of the gap flows, and narrow and wide wake structures. However, the two-cylinder flow may not be representative of flows over multiple bluff bodies because both the flows exhibit quite disparate behaviours as were explained in details by Sumner et al. (1999) and Zhang and Zhou (2001). To our best knowledge, not much attention has been paid till date to flow studies over more-than-two cylinders. Very few researchers have done experiments on multi-cylinders (more-than-two cylinders). Kang (2004) has reported detailed numerical results of three side-by-side circular cylinders. But hardly any numerical study has been so far performed on the flow past three cylinders in tandem. Therefore, numerical simulations are also performed over three circular cylinders in side-by-side and tandem arrangements with transverse and longitudinal gaps of 2D and 5D respectively at Re = 100 and 200.

In order to get better understanding of the wake interference around multiple cylinders, the flow past a single cylinder is also simulated and that solution is taken as a reference for analyzing the interaction effect for flow past multi-cylinders. The results obtained for single and two cylinder cases have been validated with the results from the existing literature.

2. Governing equations

The equations governing incompressible viscous fluid flow in two-dimensions are the Continuity equation and the two components of Momentum equation. In absence of body forces and heat transfer, these equations can be expressed in the conservative non-dimensional primitive variable form as follows:

Continuity equation:

$$\frac{\partial u}{\partial x}+\frac{\partial v}{\partial y}=0 \tag{1}$$

Momentum equations:

x-momentum:

$$\frac{\partial u}{\partial t}+\frac{\partial (u^2)}{\partial x}+\frac{\partial (uv)}{\partial y}=-\frac{\partial p}{\partial x}+\frac{1}{\mathrm{Re}}\times\left(\frac{\partial^2 u}{\partial x^2}+\frac{\partial^2 u}{\partial y^2}\right) \tag{2a}$$

y-momentum:

$$\frac{\partial v}{\partial t}+\frac{\partial(uv)}{\partial x}+\frac{\partial(v^2)}{\partial y}=-\frac{\partial p}{\partial y}+\frac{1}{\mathrm{Re}}\times\left(\frac{\partial^2 v}{\partial x^2}+\frac{\partial^2 v}{\partial y^2}\right) \tag{2b}$$

where the velocity components u and v are in the x and y-directions respectively, p is ratio of pressure and density, Re is the Reynolds number and t is the non-dimensional time.

In the present calculations, free-stream values for pressure and velocity are assigned as the initial values to each triangular cell in the domain. This physically means that the body is suddenly introduced into a uniform free-stream flow. The inlet, outlet, top and bottom boundaries of the rectangular domain are kept far away from the body surface. At all the outer boundaries free-stream Dirichlet boundary condition is applied. On the body surface no-slip condition is applied.

3. Unstructured grid based finite volume discretization of governing equations on triangular cells

To obtain a numerical solution, the governing flow equations are discretized by a finite volume technique based on the integral form of the equations to be solved. The physical region, in which the equations are solved, is divided into elementary triangular cells within which the integration is performed. Only the coordinates of the corners of the cells are necessary. In the present investigation unstructured triangular grid has been generated using GAMBIT 6.2.1® software and used as input to the solver.

For any arbitrary triangular cell as shown in Fig. 1a, Eqs. (1), (2a), and (2b) can be written in integral form as:

Continuity equation:

$$\int\int_{\Omega}\left(\frac{\partial u}{\partial x}+\frac{\partial v}{\partial y}\right)d\Omega=0 \tag{3}$$

Momentum equations:

$$\int\int_{\Omega}\left(\frac{\partial u}{\partial t}\right)d\Omega+\int\int_{\Omega}\left(\frac{\partial(uu)}{\partial x}+\frac{\partial(vu)}{\partial y}\right)d\Omega=-\int\int_{\Omega}\left(\frac{\partial p}{\partial x}\right)d\Omega+\int\int_{\Omega}\frac{1}{Re}\times\left[\frac{\partial}{\partial x}\left(\frac{\partial u}{\partial x}\right)+\frac{\partial}{\partial y}\left(\frac{\partial u}{\partial y}\right)\right]d\Omega \tag{4a}$$

$$\int\int_{\Omega}\left(\frac{\partial v}{\partial t}\right)d\Omega+\int\int_{\Omega}\left(\frac{\partial(uv)}{\partial x}+\frac{\partial(vv)}{\partial y}\right)d\Omega=-\int\int_{\Omega}\left(\frac{\partial p}{\partial y}\right)d\Omega+\int\int_{\Omega}\frac{1}{Re}\times\left[\frac{\partial}{\partial x}\left(\frac{\partial v}{\partial x}\right)+\frac{\partial}{\partial y}\left(\frac{\partial v}{\partial y}\right)\right]d\Omega \tag{4b}$$

where Ω is any two-dimensional flow domain over which the integration is performed.

Applying Green's theorem to Eqs. (3), (4a), and (4b) for any cell 'P' (Fig. 1) yields,

Continuity equation:

$$\begin{aligned}\int\int_{\Omega}\left(\frac{\partial u}{\partial x}+\frac{\partial v}{\partial y}\right)d\Omega&=\oint_{C}(u\times dy-v\times dx)\\&=(u_1\times\Delta y_{ab}-v_1\times\Delta x_{ab})+(u_2\times\Delta y_{bc}\\&\quad-v_2\times\Delta x_{bc})+(u_3\times\Delta y_{ca}-v_3\times\Delta x_{ca})\\&\quad+O(|r_{12}|^3,\ldots)=0\end{aligned} \tag{5}$$

Momentum equations:
Unsteady term:

$$\int\int_{\Omega}\left(\frac{\partial\varphi}{\partial t}\right)d\Omega=\left(\frac{\partial\varphi}{\partial t}\right)\times a_P=\left(\frac{\varphi_P^{n+1}-\varphi_P^{n}}{\Delta t}\right)\times a_P \tag{6a}$$

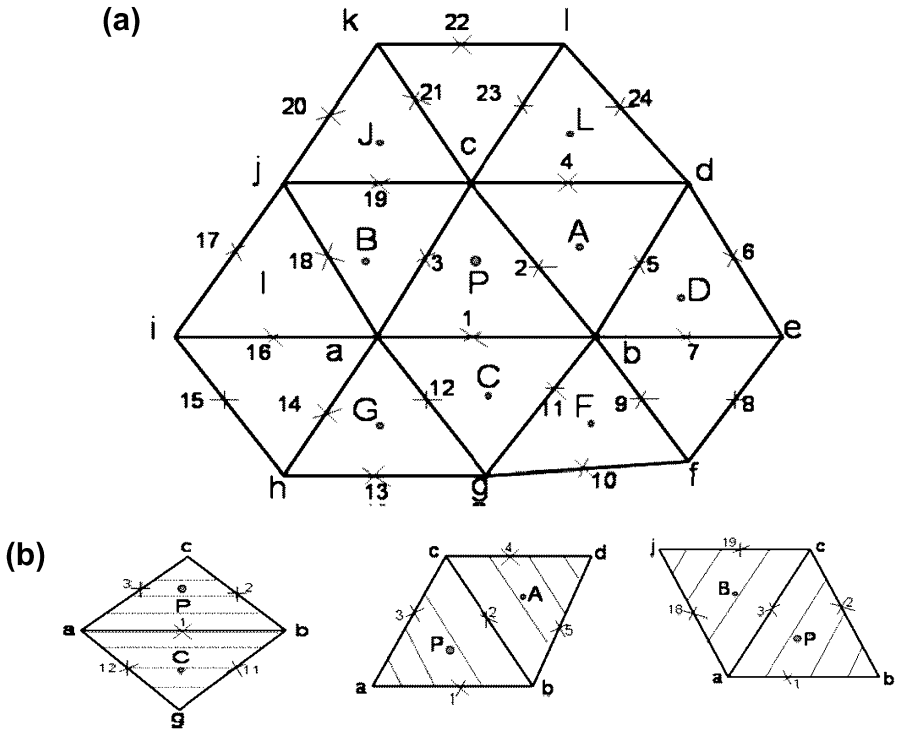

Fig. 1. Grid arrangement (a) Main control volume and (b) control volumes for calculation of cell face velocities at 1, 2 and 3 faces for triangular grid arrangement.

Convective terms:

$$\int\int_{\Omega}\left(\frac{\partial(u\varphi)}{\partial x}+\frac{\partial(v\varphi)}{\partial y}\right)d\Omega=\oint_{C}((u\varphi)\times dy-(v\varphi)\times dx)$$
$$=\left((u\varphi)_1\times\Delta y_{ab}-(v\varphi)_1\times\Delta x_{ab}\right)+\left((u\varphi)_2\times\Delta y_{bc}-(v\varphi)_2\times\Delta x_{bc}\right)+\left((u\varphi)_3\times\Delta y_{ca}-(v\varphi)_3\times\Delta x_{ca}\right)+O(|r_{12}|^3,\ldots) \quad (6b)$$

Pressure terms:

$$\int\int_{\Omega}\left(\frac{\partial p}{\partial x}\right)d\Omega=\oint_{C}p\times dy=p_1\times\Delta y_{ab}+p_2\times\Delta y_{bc}+p_3\times\Delta y_{ca}+O\left(|r_{12}|^3,\ldots\right) \quad (6c)$$

$$\int\int_{\Omega}\left(\frac{\partial p}{\partial y}\right)d\Omega=-\oint_{C}p\times dx=-\left\{p_1\times\Delta x_{ab}+p_2\times\Delta x_{bc}+p_3\times\Delta x_{ca}+O(|r_{12}|^3,\ldots)\right\} \quad (6d)$$

Diffusive terms:

$$\int\int_{\Omega}\frac{1}{Re}\times\left[\frac{\partial}{\partial x}\left(\frac{\partial\varphi}{\partial x}\right)+\frac{\partial}{\partial y}\left(\frac{\partial\varphi}{\partial y}\right)\right]d\Omega=\frac{1}{Re}\times\oint_{C}\left[\left(\frac{\partial\varphi}{\partial x}\right)\times dy-\left(\frac{\partial\varphi}{\partial y}\right)\times dx\right]$$
$$=\frac{1}{Re}\times\left[\left(\frac{\partial\varphi}{\partial x}\right)_1\times\Delta y_{ab}-\left(\frac{\partial\varphi}{\partial y}\right)_1\times\Delta x_{ab}+\left(\frac{\partial\varphi}{\partial x}\right)_2\times\Delta y_{bc}-\left(\frac{\partial\varphi}{\partial y}\right)_2\times\Delta x_{bc}+\left(\frac{\partial\varphi}{\partial x}\right)_3\times\Delta y_{ca}-\left(\frac{\partial\varphi}{\partial y}\right)_3\times\Delta x_{ca}+O(|r_{12}|^3,\ldots\right] \quad (6e)$$

where u_1, v_1, u_2, v_2, u_3 and v_3 are the cell face-centre velocities on three respective faces of a triangular cell, ϕ is the convective flux term and is equal to u and v along x- and y-directions respectively and $\frac{1}{Re}\times(\frac{\partial\varphi}{\partial x})$ and $\frac{1}{Re}\times(\frac{\partial\varphi}{\partial y})$ are the diffusive fluxes. 'C' is the contour of the cell 'P' and $O(|r_{12}|^3,\ldots)$ is the Newton–Cotes integration error. The values of velocity derivatives are obtained by using Taylor series expansion about the cell face centre points. For example, the velocity derivatives on the face '1' of the cell 'P' can be expressed as:

$$\left(\frac{\partial\varphi}{\partial x}\right)_1=\frac{(\varphi_b-\varphi_a)\times\Delta y_{CP}-(\varphi_P-\varphi_C)\times\Delta y_{ab}}{\Delta x_{ab}\times\Delta y_{CP}-\Delta x_{CP}\times\Delta y_{ab}} \quad (7a)$$

$$\left(\frac{\partial\varphi}{\partial y}\right)_1=\frac{(\varphi_b-\varphi_a)\times\Delta x_{CP}-(\varphi_P-\varphi_C)\times\Delta x_{ab}}{\Delta x_{ab}\times\Delta y_{CP}-\Delta x_{CP}\times\Delta y_{ab}} \quad (7b)$$

Δ is the spacing operator, e.g. $\Delta x_{ab}=x_b-x_a$.

In Eq. (6a), the transient term is approximated using the lumped mass approach. In this equation, the superscript of ϕ stands for the particular time step, namely nth or $(n+1)$th. Δt is the time interval. a_P represents the area of the cell P. The value of the variable at the cell centre, say ϕ_P, is used as the representative value for the entire cell for evaluating the transient term. The explicit forward Euler method has been used for the discretizing the time derivative which is first order accurate in time. Since very small time steps have been used for all calculations, this does not compromise the time accuracy to a significant extent.

4. Application of consistent flux reconstruction scheme on unstructured grid

Based on the above finite volume discretization of the governing equations, an explicit two-dimensional solver has been developed. The solver makes use of collocated grid arrangement, where the flow variables u, v and p share the same location at the centre of the cells. For the calculation of the convective and pressure fluxes through the cell faces, the unknown values (i.e. u_1, u_2, u_3, v_1, v_2, v_3, p_1, p_2 and p_3) at the centre of the cell faces need to be evaluated.

The cell face-centre velocities are obtained by using a CFR scheme based on triangular cells. The present approach involves the solution of the x and y components of momentum equations at the centre of the faces of the each cell. This provides the solution for the required cell face-centre velocities u_1, v_1, u_2, v_2, u_3 and v_3 for flux calculation. These values are then substituted into the discrete continuity equation to obtain the discrete Poisson equation for pressure. In order to maintain the accuracy of the finite volume discretization, the cell face velocities are approximated by a second-order accurate closure method. The cell face-centre pressures are obtained by linearly interpolating the cell centre pressure values calculated by solving the pressure-Poisson equation.

When the cell face velocities are obtained by linear interpolation, the cell face velocity e.g. u_1, on the face '1', comes as a function of the cell centre values of the u-velocity component of the concerned cell and its neighbours, but is independent of the corresponding v-velocity component and pressure. Although upwind interpolation schemes can be used to circumvent the numerical instability problems, spurious pressure modes exist when such linear interpolation formulae are implemented on collocated grids. One of the most effective means to overcome this difficulty is to use a physically consistent flux reconstruction approach by which the cell face velocities are expressed not only in terms of the dependent variable u, in this case, but also other physical quantities v and p.

In the present solver, a fully explicit scheme is adopted for the reconstruction of cell face velocities as well as for updating the flow variables at the cell centres. A 10-point stencil is used for both pressure and velocity calculations. For calculating the viscous fluxes on the face '1' (flux reconstruction cell centered about '1', comprising of cells P and C, Fig. 1), the values of velocities at points 'a', 'g', 'b' and 'c' are necessary. For updating the flow variables at the cell centres, the momentum equations are solved in an explicit manner. The layout of the flux reconstruction cells used in the present solver is different from that of Roy and Bandyopadhyay (2006). The present flux reconstruction cells are chosen in such a manner that the integration points for the main control volume and the reconstruction control volume coincide; therefore it reduces the computational effort.

The closures of the cell face velocities u_1, v_1, u_2, v_2, u_3 and v_3 are obtained from the discretized u and v components of the momentum equations for reconstruction control volumes defined around the points '1', '2' and '3' respectively are shown in Fig. 1b. The finite-volume schemes used at these points are similar to that used at point 'P'. The discretizations of the various terms in the x-component of momentum equation are given as follows:

Unsteady term:

$$\int\int_{\Omega_1}\left(\frac{\partial u}{\partial t}\right)_1 d\Omega_1=\left(\frac{\partial u}{\partial t}\right)_1 a_1=\left(\frac{u_1^{n+1}-u_1^n}{\Delta t}\right)\times(a_P+a_C) \quad (8a)$$

Convective term:

$$\int\int_{\Omega_1}\left(\frac{\partial(uu)}{\partial x}+\frac{\partial(vu)}{\partial y}\right)_1 d\Omega_1 = \oint_{C_1}((uu)\times dy-(vu)\times dx)$$
$$= u_{11}^2\times\Delta y_{gb}-u_{11}\times v_{11}\times\Delta x_{gb} + u_2^2\times\Delta y_{bc}-u_2\times v_2\times\Delta x_{bc} + u_3^2\times\Delta y_{ca}-u_3\times v_3\times\Delta x_{ca} + u_{12}^2\times\Delta y_{ag}-u_{12}\times v_{12} \times\Delta x_{ag}+O(|r_{12}|^3,\ldots)$$
$$= UCFLUX_1 \quad (8b)$$

Pressure term:

$$\int\int_{\Omega_1}\left(\frac{\partial p}{\partial x}\right)_1 d\Omega_1 = \oint_{C_1} p dy$$
$$= p_{11}\times\Delta y_{gb}+p_2\times\Delta y_{bc}+p_3\times\Delta y_{ca}+p_{12}\times\Delta y_{ag}$$
$$= UPFLUX_1 \quad (8c)$$

Diffusive term:

$$\int\int_{\Omega_1}\left[\frac{\partial}{\partial x}\left(\frac{\partial u}{\partial x}\right)+\frac{\partial}{\partial y}\left(\frac{\partial u}{\partial y}\right)\right]_1 d\Omega_1$$
$$= \oint_{C_1}\left[\left(\frac{\partial u}{\partial x}\right)\times dy-\left(\frac{\partial u}{\partial y}\right)\times dx\right]$$
$$= \left(\frac{\partial u}{\partial x}\right)_{11}\times\Delta y_{gb}+\left(\frac{\partial u}{\partial x}\right)_2\times\Delta y_{bc}+\left(\frac{\partial u}{\partial x}\right)_3\times\Delta y_{ca} + \left(\frac{\partial u}{\partial x}\right)_{12}\times\Delta y_{ag}-\left(\frac{\partial u}{\partial y}\right)_{11}\times\Delta x_{gb}-\left(\frac{\partial u}{\partial y}\right)_2\times\Delta x_{bc} - \left(\frac{\partial u}{\partial y}\right)_3\times\Delta x_{ca}-\left(\frac{\partial u}{\partial y}\right)_{12}\times\Delta x_{ag}+O(|r_{12}|^3,\ldots)$$
$$= UDFLUX_1 \quad (8d)$$

In Eq. (8a), the 'lumped mass' approach has been applied to the flux reconstruction cell on the face '1' of the cell *P*. The area of the reconstruction cell is the sum of the areas of cells *P* and *C*. The value of the variable at the reconstruction cell centre, namely u_1, is used as the representative value for the entire reconstruction cell for evaluating the transient term. Ω_1 is the domain of the '1' cell and C_1 is the contour enclosing it. The values of the properties at various nodal points like *a*, *b*, *c*, etc. are obtained by linear interpolation of neighbouring cell centre property values. For example, the equation used for evaluating the value of the property at node '*a*' is given as follows:

$$\varphi_a=\frac{\sum_i\left(\frac{\varphi_P[i]}{d[i]}\right)}{\sum_i\left(\frac{1}{d[i]}\right)} \quad (9)$$

where $\phi_P[i]$ is the cell centre value of any of the neighbouring cells of node '*a*'. $d[i]$ is the distance of the neighbouring cell-centre from node '*a*'. The number of neighbours (i) can vary from node to node. The first order velocity derivatives ($\partial\phi/\partial x$) and ($\partial\phi/\partial y$) at points 2, 3, 11 and 12 are obtained using Taylor series expansion as explained in Eqs. (7a) and (7b). The velocity derivatives at the other integration points and on other faces of cell '*P*' (2 and 3) are calculated using similar formulae. The closure interpolation formulae for u_1 can be derived from the substitution of Eqs. (8a), (8b), (8c), (8d) into Eq. (4a). The resulting expression for u_1 at the $(n+1)$th time level is:

$$u_1^{n+1}=u_1^n+\frac{1}{(a_P+a_C)}\times\left(-UCFLUX_1-UPFLUX_1+\left(\frac{1}{\mathrm{Re}}\right)\times UDFLUX_1\right)\times\Delta t \quad (10)$$

The cell face velocity at *n*th time level i.e. u_1^n is taken as the linear interpolation of the adjoining cell centre values at that time level. In a similar manner Eqs. (4a) and (4b) are solved to obtain the flux closure relationships for v_1, u_2, v_2, u_3 and v_3 respectively at the $(n+1)$th time level.

At the body boundary cells no velocity reconstruction is necessary on the faces lying on the body surface as no-slip boundary condition is applied over such faces. For reconstruction on the other two faces, the calculations are done with due care by enforcing no-slip at all the nodal points which lie on the body boundary. The values of pressure at all the body boundary points are obtained from the neighbouring flow field points by applying zero normal pressure gradient condition. The velocity derivatives on the body boundary are calculated by assuming a layer of ghost cells below the body, where properties at each node of a ghost cell which are not located on the body surface are equal in magnitude but opposite in sign to the corresponding nodal value of the body boundary cell. At the outer boundary, solutions of the discretized flux reconstruction equations are obtained on the basis of the free stream values.

5. The pressure-Poisson equation

The equation for pressure is obtained by substituting the expressions for u_1^{n+1}, v_1^{n+1}, u_2^{n+1}, v_2^{n+1}, u_3^{n+1} and v_3^{n+1} into the discrete continuity equation (Eq. (5)). The following pressure-Poisson equation is obtained with pressure as unknown:

$$p_P=\frac{1}{C_P}\times\begin{bmatrix}SOURCE-C_A\times p_A-C_B\times p_B-C_C\times p_C-C_D\times p_D\\ -C_F\times p_F-C_G\times p_G-C_I\times p_I-C_J\times p_J-C_L\times p_L\end{bmatrix} \quad (11)$$

where the coefficients C_P, C_A, C_B, C_C, C_D, C_F, C_G, C_I, C_J and C_L are the geometrical parameters of the cells and SOURCE is the total source term comprising of the cell divergence at the *n*th time level, D_i^n, and the convective and diffusive fluxes at the cell faces. The term SOURCE is an explicit function of the nodal variables u_i and v_i which include the concerned cell and its nine neighbours as follows:

$$SOURCE=\left(\frac{1}{\Delta t}\right)\times\begin{pmatrix}u_1\times\Delta y_{ab}+u_2\times\Delta y_{bc}+u_3\times\Delta y_{ca}\\ -v_1\times\Delta x_{ab}-v_2\times\Delta x_{bc}-v_3\times\Delta x_{ca}\end{pmatrix}^n + \left(\frac{\Delta y_{ab}}{a_P+a_C}\right)\times(-UCFLUX_1+\left(\frac{1}{\mathrm{Re}}\right)\times UDFLUX_1) + \left(\frac{\Delta y_{bc}}{a_P+a_A}\right)\times(-UCFLUX_2+\left(\frac{1}{\mathrm{Re}}\right)\times UDFLUX_2) + \left(\frac{\Delta y_{ca}}{a_P+a_B}\right)\times(-UCFLUX_3+\left(\frac{1}{\mathrm{Re}}\right)\times UDFLUX_3) - \left(\frac{\Delta x_{ab}}{a_P+a_C}\right)\times(-VCFLUX_1+\left(\frac{1}{\mathrm{Re}}\right)\times VDFLUX_1) - \left(\frac{\Delta x_{bc}}{a_P+a_A}\right)\times(-VCFLUX_2+\left(\frac{1}{\mathrm{Re}}\right)\times VDFLUX_2) - \left(\frac{\Delta x_{ca}}{a_P+a_B}\right)\times(-VCFLUX_3+\left(\frac{1}{\mathrm{Re}}\right)\times VDFLUX_3) \quad (12)$$

where expressions for $UCFLUX_1$ and $UDFLUX_1$ are provided in Eqs. (8b) and (8d) respectively. The expressions for the remaining flux terms are similarly obtained from the other cell face centres.

Eq. (11) is used directly as the pressure equation to determine the pressure field. For the cells near the body boundary, the expression for the pressure equation is obtained by applying the zero velocity boundary condition in the discretized continuity equation. Zero normal pressure gradient across the body boundary is applied in Eq. (11). Pressure on the body boundary is obtained by using the above Neumann boundary condition and special care is taken to satisfy the compatibility condition (Abdallah, 1987a,b) in the discretized pressure-Poisson equation for such cells. Satisfaction of the compatibility condition ensures that there is zero net source term when the discretized equations over the entire computational domain are considered. Dirichlet boundary condition of free stream values has been applied in the outer boundary of the flow

domain. Gauss–Siedel method has been used for the iterative solution of the pressure-Poisson equation. Once the pressure-Poisson equation is solved, the cell centre pressure values are available. The cell face-centre pressures are obtained by linear interpolation of adjacent cell centre values. For example, cell face-centre pressure on face '1' is obtained as:

$$p_1 = \frac{p_C \times a_P + p_P \times a_C}{a_P + a_C} \tag{13}$$

The discretized cell centre momentum equations are solved by substituting the values of velocity derivatives at cell face-centres, interpolated cell face-centre pressures, and the values of the cell face-centre velocities obtained by the CFR approach as formulated in the present investigation. From these equations, the velocities at the cell centres are updated explicitly.

6. Geometrical description of the flow domain

The geometrical description of two and three cylinder configuration with cylinders of equal diameter D is defined by two parameters: the transverse gap T and the longitudinal gap L based on centre-to-centre distances as indicated in Fig. 2. The top and bottom boundaries are kept at a transverse distance of 15 times of the cylinder diameter from the central cylinder so that blockage ratio for different multi-cylinder cases is always less than 10%. The in-flow boundary is kept at a distance of 10 times of the cylinder diameter from the centre of the front cylinder. The out-flow boundary is kept at a distance of 25 times of the cylinder diameter downstream from the centre of the rear cylinder.

7. Initial condition and boundary conditions

The governing equations for viscous incompressible flow are mixed parabolic–elliptic in nature. The solution marches forward in time due to the parabolic behaviour and disturbances may travel along any direction, upstream or downstream due to the elliptic behaviour. Therefore initial conditions need to be set at the beginning of the solution and boundary conditions surrounding the domain should be specified.

In the beginning of the solution process, uniform free-stream velocity and pressure field are prescribed in each cell of the flow domain as given below:

$$\left.\begin{aligned} u[i] &= u_\infty \\ v[i] &= v_\infty \\ p[i] &= p_\infty \end{aligned}\right\} \quad \text{for all triangular cells in the flow domain} \tag{14}$$

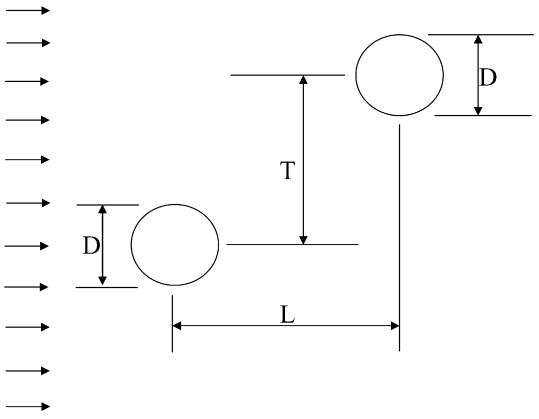

Fig. 2. Problem description.

This physically means that the body is suddenly introduced into a uniform free-stream flow. Free-stream parameters are indicated by suffix ∞. In the present calculations unconfined flow past single and multiple circular cylinders has been considered. For the rectangular flow domain, the inlet, outlet, top boundary and bottom boundary are kept far away from the body surface. At all the outer boundaries, free stream Dirichlet boundary condition is applied. On the body surface, no slip condition is used.

8. Results and discussion

In this study, the unstructured CFR method is applied to simulate flows around single, two and three circular cylinders within the low Reynolds number range, i.e. Re = 100 and 200. For numerical simulation of this flow problem, it is necessary to visualize the details of the computed flow around the cylinders and in their near wake region. Therefore, streamlines and vorticity contours are plotted as the flow visualization aids. Some parameters characterizing the flow aspects such as lift and drag coefficients and Strouhal number are also computed and quantitatively compared with the results of other researchers. The results obtained for single cylinder were primarily used for validating the present CFRUNS solver. To analyze and better understand the vortex shedding behaviour and the interference of vortex streets behind multi-cylinders, the solution of flow past single cylinder has often been used as a reference for comparison.

8.1. Flow past a single circular cylinder

Flow past an isolated circular cylinder has attractive features like vortex shedding behind the cylinder and the periodic variation of the flow field at moderate Reynolds number. In the present study, the unsteady flow at Re = 100 and 200 are simulated on a triangular mesh comprising of 29,464 cells and 14,878 nodes out of which 160 nodes are on the body surface. The size of the grid has been decided based on a grid independence study carried out on four different grids. The difference in the grids is based on the number of nodes on the cylinder surface. Table 1 gives the details of the grid independence test carried out at Re = 100. The distribution of the cells in the domain can be seen in Fig. 3a. The non-dimensional time step used in the calculation is 0.001. At every time level, the convergence criteria for pressure-Poisson equation is set in a manner that the residual is less than 10^{-6}. The initial convergence pattern of the numerical scheme for flow past a single circular cylinder at Re = 100 is shown in Fig. 3b. The convergence characteristics of the scheme was tested for several other problems and found to be satisfactory. To obtain the characteristics of lift and drag coefficients, simulation was performed up to 400 non-dimensional time.

Based on the variation of the values of lift coefficients, drag coefficients and Strouhal number, Grid 3 has been chosen for the flow calculations. For multi-cylinder simulations also same number of nodes is chosen on the body surface for each cylinder.

Fig. 3c and d shows the vorticity contours and streamlines past a single cylinder for Re = 100 and 200 respectively at instantaneous time t = 400. The Karman vortex street is well established in both

Table 1
Grid independence test carried out at Re = 100.

Number of nodes on the body	Drag coefficient (CD)	Lift coefficient (CL)	Strouhal number (St)
80 (Grid 1)	1.112 ± 0.021	±0.181	0.168
120 (Grid 2)	1.185 ± 0.015	±0.21	0.164
160 (Grid 3)	1.352 ± 0.010	±0.278	0.161
200 (Grid 4)	1.381 ± 0.010	±0.281	0.161

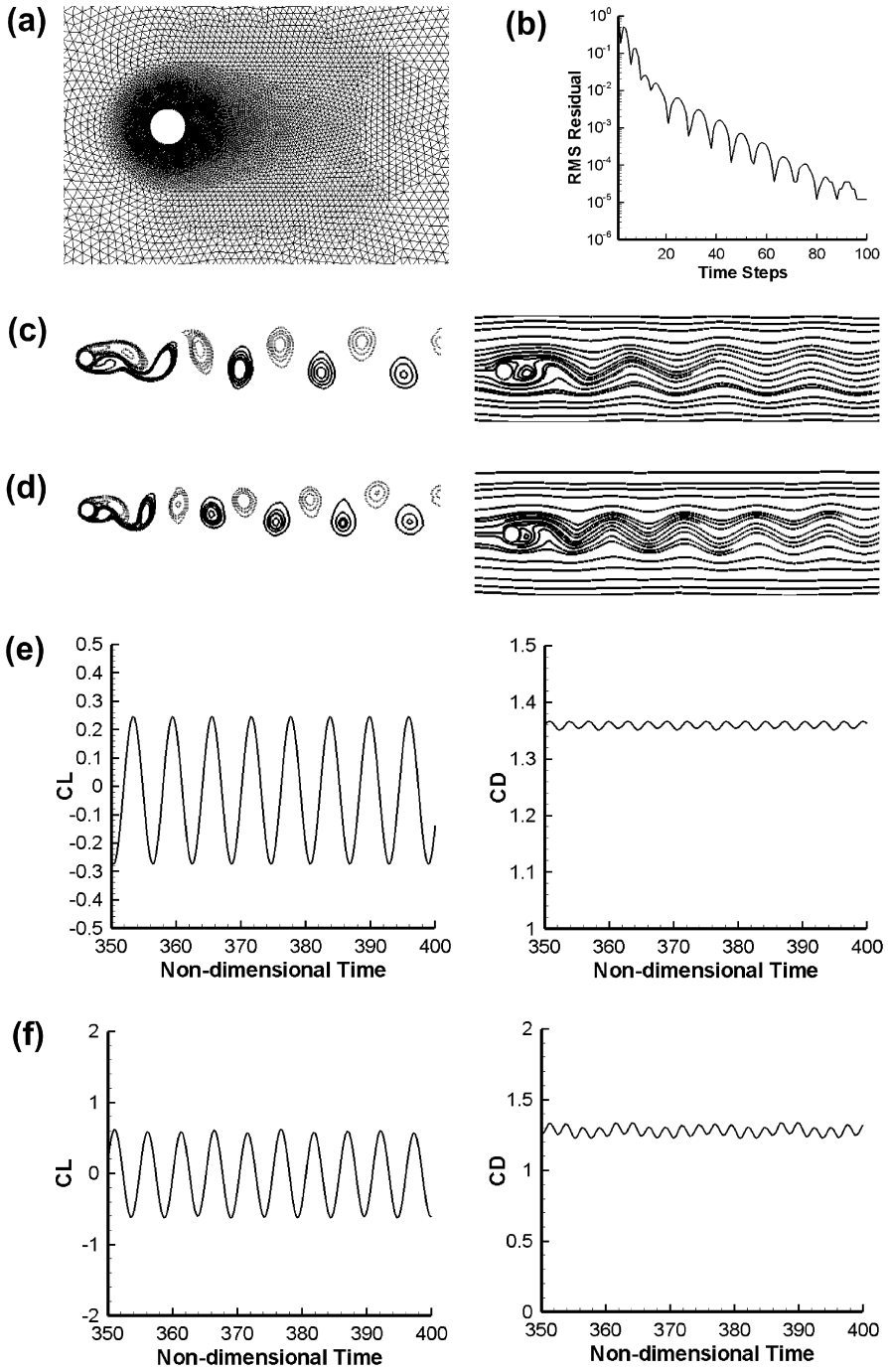

Fig. 3. (a) Close-up view of the triangular unstructured mesh around a single circular cylinder, (b) Initial convergence pattern of the numerical scheme for flow past a single circular cylinder at Re = 100, (c) Vorticity contours and streamlines of flow past single circular cylinder at Re = 100, (d) Vorticity contours and streamlines of flow past single circular cylinder at Re = 200, (e) Lift and drag coefficients of flow past single circular cylinder at Re = 100, (f) Lift and drag coefficients of flow past single circular cylinder at Re = 200.

the cases. Fig. 3e and f shows the time dependent behaviour of the lift and drag coefficients on the surface of the cylinder at Re = 100 and 200. The clear periodicity illustrated in lift and drag coefficients implies the periodic vortex shedding from the rear surface of the cylinder. Table 2 lists the mean value and amplitude of drag and lift coefficients and Strouhal number of present results as well as numerical results of Meneghini et al. (2001), Ding et al. (2007), Braza et al. (1986) and Gresho et al. (1980) and the experimental results of Tritton (1959) and Wiesenberger (1921). It is observed that our results agree reasonably well with those reported by other researchers. However, it has been observed that our numerical values of drag coefficient are generally higher than the experimental values of Tritton (1959) and Wiesenberger (1921) but are marginally lower than the numerical results of Meneghini et al. (2001), Ding et al. (2007), Braza et al. (1986) and Gresho et al. (1980). Also, the Strouhal number, which is the dimensionless frequency of vortex shedding, obtained by the present numerical model lies in-between the experimental values of Friehe (1980) and Roshko (1954) and the other numerical results (Meneghini et al., 2001; Ding et al., 2007; Gresho et al., 1980). The variation of drag coefficient and

Table 2
Values of flow parameters for flow field around single circular cylinder at Re = 100 and 200.

Parameters	Drag coefficient (CD)		Lift coefficient (CL)		Strouhal number (St)	
Reynolds number	Re = 100	Re = 200	Re = 100	Re = 200	Re = 100	Re = 200
Meneghini et al. (2001)	1.370 ± 0.010	1.30 ± 0.05	–	–	0.165	0.196
Ding et al. (2007)	1.356 ± 0.010	1.348 ± 0.05	±0.287	±0.659	0.166	0.196
Braza et al. (1986)	1.364 ± 0.015	1.40 ± 0.05	±0.25	±0.75	0.160	0.200
Tritton (1959)	1.320 ± 0.010	–	–	–	0.160	–
Wiesenberger (1921)	1.326 ± 0.010	–	–	–	0.1608	–
Gresho et al. (1980)	1.816 ± 0.010	–	–	–	0.18	–
Present result	1.352 ± 0.010	1.32 ± 0.05	±0.278	±0.602	0.161	0.192

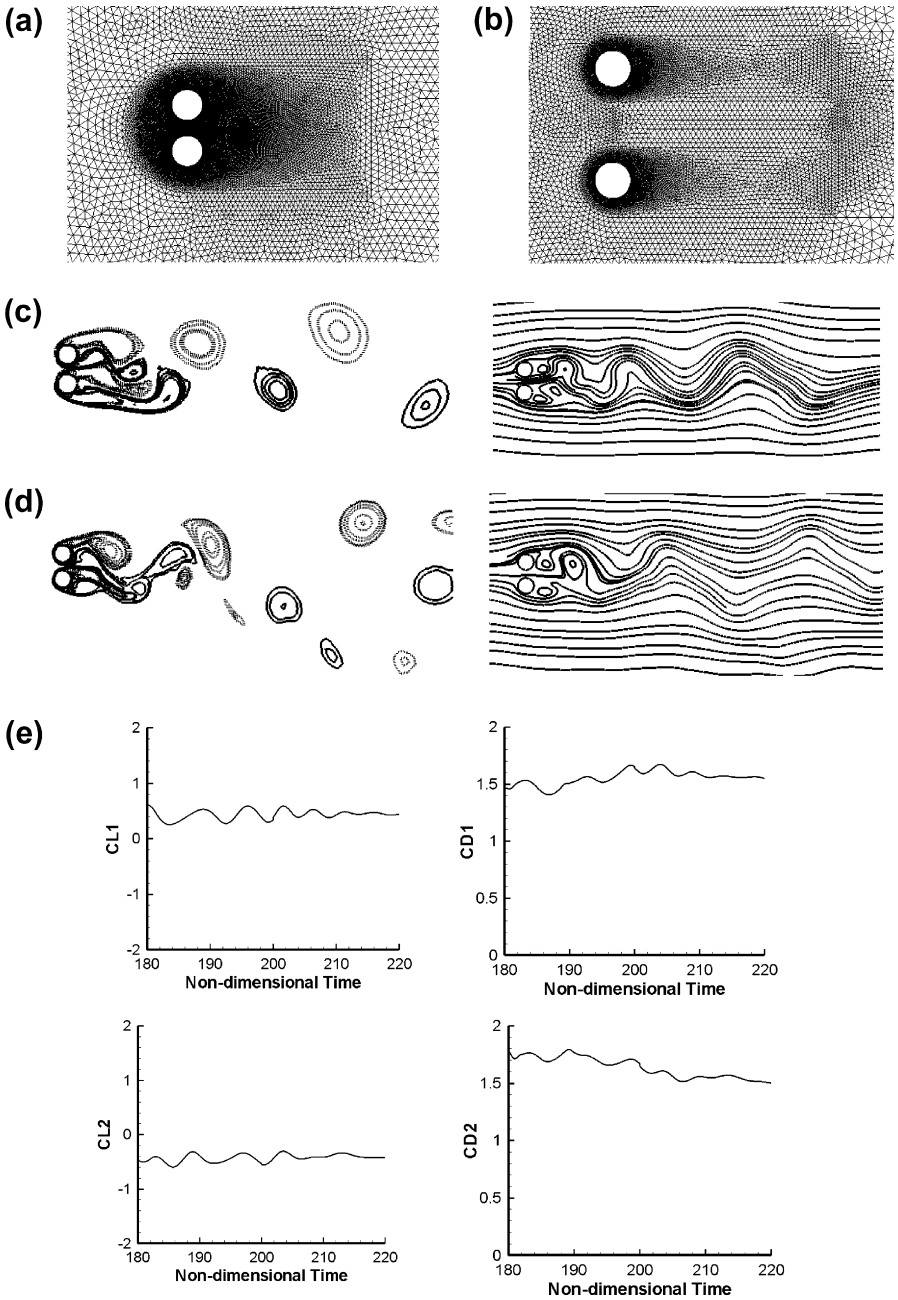

Fig. 4. (a) Close-up view of the triangular mesh around a pair of circular cylinders with $T = 1.5D$, (b) Close-up view of the triangular mesh around a pair of circular cylinders with $T = 3D$, (c) Vorticity contours and streamlines of flow past a pair of side-by-side circular cylinders ($T = 1.5D$) at Re = 100, (d) Vorticity contours and streamlines of flow past a pair of side-by- side circular cylinders ($T = 1.5D$) at Re = 200, (e) Lift and drag coefficients of flow past a pair of circular cylinders ($T = 1.5D$) at Re = 100, (f) Lift and drag coefficients of flow past a pair of circular cylinders ($T = 1.5D$) at Re = 200.

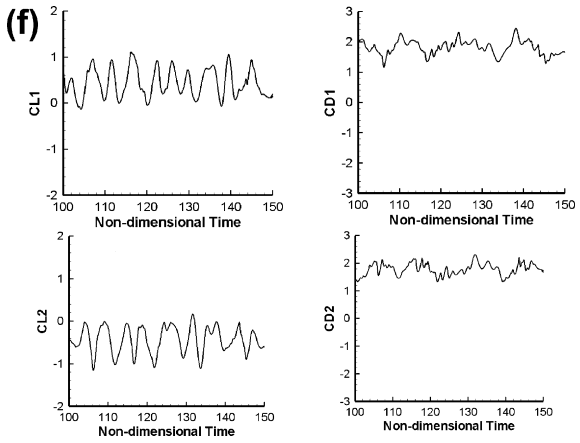

Fig. 4 (*continued*)

Strouhal number from the experimental values is probably due to the relatively coarser grid used downstream of the cylinder and the absence of three-dimensional effects in the present simulation unlike experiments. The satisfactory performance of the CFRUNS solver in solving flow past a single circular cylinder provided the necessary confidence to carry out the study of flow around two and three circular cylinders.

8.2. Flow past two side-by-side circular cylinders

Flow past two circular cylinders is much more complicated as compared to that of flow past a single circular cylinder especially when interference effects are severe. In the present study, the numerical results obtained for flow field behind two side-by-side cylinders are highlighted. In the side-by-side arrangement of two circular cylinders, numerical simulations have been performed for the cases of $T = 1.5D$ and 3D respectively. Unsteady flow at Re = 100 and 200 are simulated on a triangular mesh with 40,972 cells and 20,711 nodes for $T = 1.5D$ case and with 31,581 cells and 16,016 nodes for $T = 3D$ case respectively. The distribution of the cells in the domain can be seen in Fig. 4a and b respectively. The non-dimensional time step used for the calculation is 0.0005. At every time level, the convergence criteria for pressure-Poisson equation is set by maximum cell residual 10^{-6}. Note that flow has been assumed to be two-dimensional at the given Reynolds numbers for any transverse distance between the cylinders.

Fig. 4c and d presents the vorticity contours and streamlines of the flow field around two cylinders for $T = 1.5D$, Re = 100 and 200 respectively at instantaneous non-dimensional time $t = 150$. It is observed that the flow pattern is bistable with narrow and wide wakes behind the cylinders. This result agrees well with the experimental result of Zdravkovich (1977) who observed biased flow pattern when the transverse gap between the cylinders is within the critical gap ($1.1D < T < 2.2D$). Fig. 4e and f shows the temporal histories of drag and lift coefficients. From these figures, it can be observed that drag and lift coefficients exhibit irregular variation with time and the flow is not periodic and is drastically unsteady. Previous experimental studies of Zhou et al. (2000) and Xu et al. (2003) have reported that the flow between two cylinder surfaces (gap flow) is deflected to the side of higher-frequency cylinder and the cylinder experiences a higher drag than the other. Such relationship with regard to gap-flow direction and drag coefficient is also demonstrated numerically in the present results. It is shown that both the cylinders take irregular turns in experiencing the higher drag coefficient, indicating that the two wakes randomly flip-flop between two states of gap-flow direction. Thus, a flip-flopping wake pattern is observed. Due to the deflection of gap flow, one narrow wake region is formed behind the cylinder towards which the gap flow deflects and one wide wake region is formed behind the other cylinder. This type of flip-flopping pattern of the wake is also observed in the numerical simulation of Kang (2003) at the same transverse gap $T = 1.5D$. There is no indication of any repeatability in the lift and drag patterns with respect to time even at the lower Reynolds number. The results for the two cylinders are indicated by associating a number along with CL and CD. '1' stands for the lower cylinder and '2' stands for the upper cylinder.

Fig. 5a and b presents the vorticity contours and streamlines for the flow field past two cylinders for $T = 3D$, Re = 100 and 200 respectively at instantaneous non-dimensional time $t = 140$. Zdravkovich (1977) experimentally observed that when the transverse gap is larger than 2D, two synchronized Karman vortex streets are observed for the side-by-side arrangement of the cylinders. In our present study also vortex streets are clearly developed for this transverse gap. The time evolution of lift and drag coefficients are shown in Fig. 5c and d at Re = 100 and 200 respectively. The synchronized variation of lift and drag coefficients with time confirms the fully periodic behaviour of vortex shedding from the upper and lower cylinders. According to the time traces, the drag coefficients for both the cylinders are almost same and the lift coefficients are in-phase. The drag coefficients are out of phase at Re = 100 and consequently an in-phase-synchronized wake pattern is formed. The instantaneous flow field suggests that the vortex shedding from both cylinders occurs at nearly the same phase, pairs of like-signed vortices merge, and then some distance downstream the merging process ceases. This type of wake pattern is very well comparable with the wake patterns obtained by Kang (2003) at same transverse gap between the cylinders. On the other hand, at Re = 200, the drag and lift coefficients for both the cylinders are in anti-phase and thus, an anti-phase-synchronized wake pattern is observed. Also, the instantaneous flow field suggests that the flow is symmetric with respect to the centerline ($y = 0$) all the way far downstream. Thus, it is observed that the flow Reynolds number and the transverse gap between the cylinders influence the flow pattern downstream of the cylinders but the later plays a major role in deciding the wake patterns. It is also observed that the variation of amplitudes increase with increase in Reynolds number for lower gaps.

Table 3 mentions the mean value and amplitude of drag and lift coefficients and the Strouhal number for two cylinders at two different transverse gaps ($T = 1.5D$ and 3D) at Re = 100 and 200. It can be observed that the mean value of the lift coefficient is positive for the lower cylinder and negative for the upper cylinder. The values are larger at smaller gap which indicates that there is a stronger transverse suction effect when the cylinders are in close proximity. For the flip-flopping wake pattern at $T = 1.5D$, the fully developed flows are not periodic. Consequently, the FFT of the lift coefficients does not result in any distinctive dominant frequency, rather the vortex frequencies are irregularly scattered over a broadband frequency range, implying that multiple frequencies are intricately involved. Therefore, the Strouhal number values are not mentioned in our results for $T = 1.5D$. Only mean values of drag and lift coefficients obtained by time averaging over a substantial time period are mentioned for $T = 1.5D$ in Table 3. This would be noticed for certain cases included in Tables 4–6 also. It can also be observed that the values of the flow parameters tend towards those of a single cylinder as gap increases. It indicates that the flow interference reduces as the two cylinders are placed further apart.

Tables 4 and 5 present the comparison of present numerical results with those of Ding et al. (2007). From the comparison, it can be seen that the lift coefficients and Strouhal numbers are in good agreement with the available data. The drag coefficient does not compare very satisfactorily.

8.3. Flow past three circular cylinders

Flow past three circular cylinders is still more complicated as compared to flow field past a single cylinder or two cylinders due to more complex interference effects. Kang (2004) has reported detailed numerical results of three side-by-side circular cylinders. But hardly any numerical study has so far been performed on the flow past three cylinders in tandem. In the present study, flow field around three cylinders placed in side-by-side and tandem arrangement are reported. Apparently, this flow is more complicated than the two-cylinder flow; for example, there are two gap flows that may deflect in various ways, consequently involving more types of wake patterns as reported by Zhang and Zhou (2001). In addition the flow is more representative of flows over multiple bluff bodies of engineering interest. All the flows involving three circular cylinders considered in the present study are assumed to be two-dimensional and laminar even if they are not perfectly so at relatively higher Reynolds number and small gap spacings between the cylinders.

8.3.1. Case I: side-by-side ($T = 2D$) and tandem ($L = 2D$) arrangement

In the side-by-side and tandem arrangement of three circular cylinders, numerical simulations have been performed for the case of $T = 2D$ and $L = 2D$ respectively. The distribution of cells in the flow domain is shown in Fig. 6a. In both the cases, the time step used for the calculation is 0.0005. A triangular mesh with 40,356 cells and 20,453 nodes for $T = 2D$ case and 28,338 cells and 14,447 nodes for $L = 2D$ case have been used respectively.

Fig. 6b and c presents the vorticity contours and streamlines of flow past three side-by-side cylinders for $T = 2D$ at Re = 100 and 200 respectively at instantaneous non-dimensional time $t = 180$. It is observed that since the transverse gap (2D) falls within the range of intermediate critical gap, bistable flow pattern with narrow and wide wakes is formed behind the cylinders. This result agrees well with the experimental result of Bearmann and Wadcock (1973) and Williamson (1985) who observed biased flow pattern when the transverse gap between the cylinders is within the critical gap ($1.1D < T < 2.2D$). Fig. 6d and e shows the temporal histories of drag and lift coefficients. From these figures, it can be observed that drag and lift coefficients exhibit irregular variation with time. It implies that irregular vortex shedding occurs behind the sets of cylinders. Thus, it is evident that the flow is no longer periodic and becomes drastically unsteady. This type of flow structure evolves flip-flopping wake pattern. Kang (2004) had also observed similar wake pattern for similar gap spacing between cylinders. Moreover, two types of flip-flopping wake patterns are

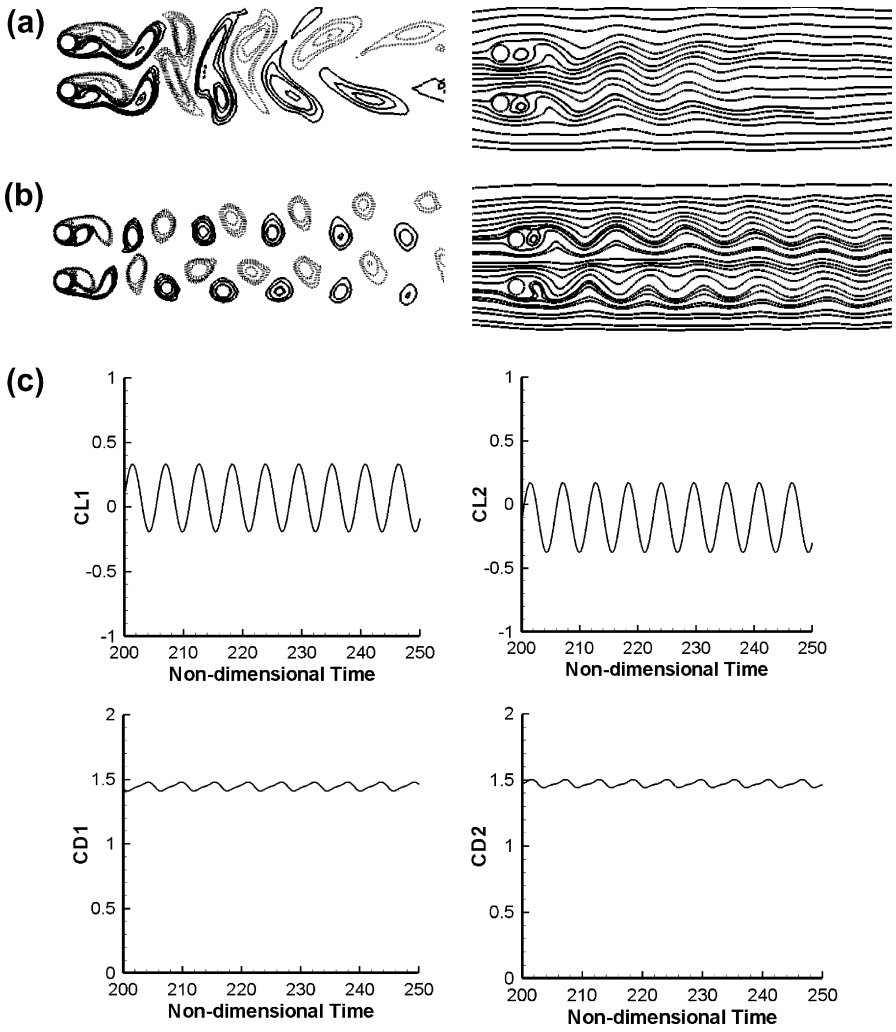

Fig. 5. (a) Vorticity contours and streamlines of flow past a pair of side-by-side circular cylinders ($T = 3D$) at Re = 100, (b) Vorticity contours and streamlines of flow past a pair of side-by- side circular cylinders ($T = 3D$) at Re = 200, (c) Lift and drag coefficients of flow past a pair of circular cylinders ($T = 3D$) at Re = 100, (d) Lift and drag coefficients of flow past a pair of circular cylinders ($T = 3D$) at Re = 200.

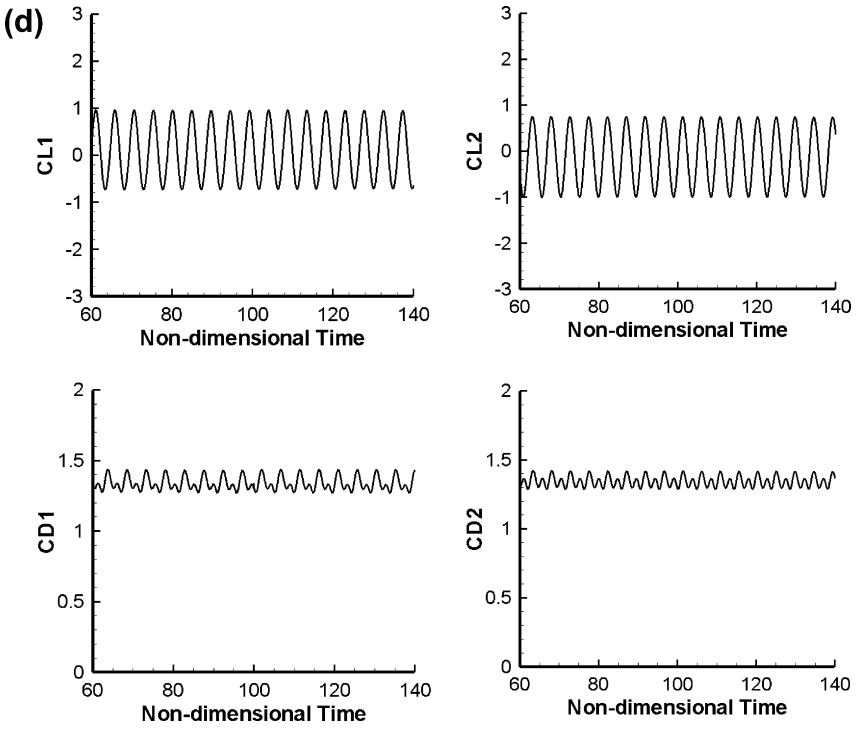

Fig. 5 (*continued*)

Table 3
Values of flow parameters for flow around two side-by-side circular cylinders at Re = 100 and 200.

Parameters		Drag coefficient (CD)		Lift coefficient (CL)		Strouhal number (St)	
Reynolds number		Re = 100	Re = 200	Re = 100	Re = 200	Re = 100	Re = 200
T = 1.5D	Upper Cylinder	1.58	1.68	−0.41	−0.5	–	–
	Lower Cylinder	1.52	1.60	0.41	0.5	–	–
T = 3D	Upper Cylinder	1.45 ± 0.05	1.35 ± 0.05	−0.1 ± 0.025	−0.1 ± 0.8	0.181	0.211
	Lower Cylinder	1.45 ± 0.05	1.35 ± 0.05	0.1 ± 0.025	0.1 ± 0.8	0.181	0.211

Table 4
Comparison of flow parameter values for two side-by-side circular cylinders at Re = 100.

Parameters		Drag coefficient (CD)		Lift coefficient (CL)		Strouhal number(St)	
Results		Present result	Ding et al. (2007)	Present result	Ding et al. (2007)	Present result	Ding et al. (2007)
T = 1.5D	Upper Cylinder	1.58	1.53	−0.41	−0.46	–	–
	Lower Cylinder	1.52	1.51	0.41	0.47	–	–
T = 3D	Upper Cylinder	1.45 ± 0.05	1.56 ± 0.03	−0.1 ± 0.025	−0.131 ± 0.253	0.181	0.182
	Lower Cylinder	1.45 ± 0.05	1.56 ± 0.03	0.1 ± 0.025	0.131 ± 0.253	0.181	0.182

Table 5
Comparison of flow parameter values for two side-by-side circular cylinders at Re = 200.

Parameters		Drag coefficient (CD)		Lift coefficient (CL)		Strouhal number (St)	
Results		Present result	Ding et al. (2007)	Present result	Ding et al. (2007)	Present result	Ding et al. (2007)
T = 1.5D	Upper Cylinder	1.68	1.54	−0.5	−0.41	–	–
	Lower Cylinder	1.60	1.52	0.5	0.43	–	–
T = 3D	Upper Cylinder	1.35 ± 0.05	1.548 ± 0.03	−0.1 ± 0.8	−0.104 ± 0.866	0.211	0.215
	Lower Cylinder	1.35 ± 0.05	1.548 ± 0.03	0.1 ± 0.8	0.104 ± 0.866	0.211	0.215

observed in the gap spacing ranges as suggested by Kang (2004): one is that the two gap flows run downstream (nearly) parallel to each other and the other is that the two gap flows run towards free stream, leading to narrow wakes behind the two outer cylinders and a wide wake behind the central one. In the former pattern (parallel mode), the drag coefficient for the central cylinder is much higher than those for the two outer cylinders. In the later pattern (symmetric mode), the drag coefficient for the central cylinder drops comparable to those for the two others. It has been observed from the vorticity contours in Fig. 6 that the parallel flip-flopping wake pattern bifurcates to deflected pattern as the vortices deflect towards the vortices behind upper cylinder. This phe-

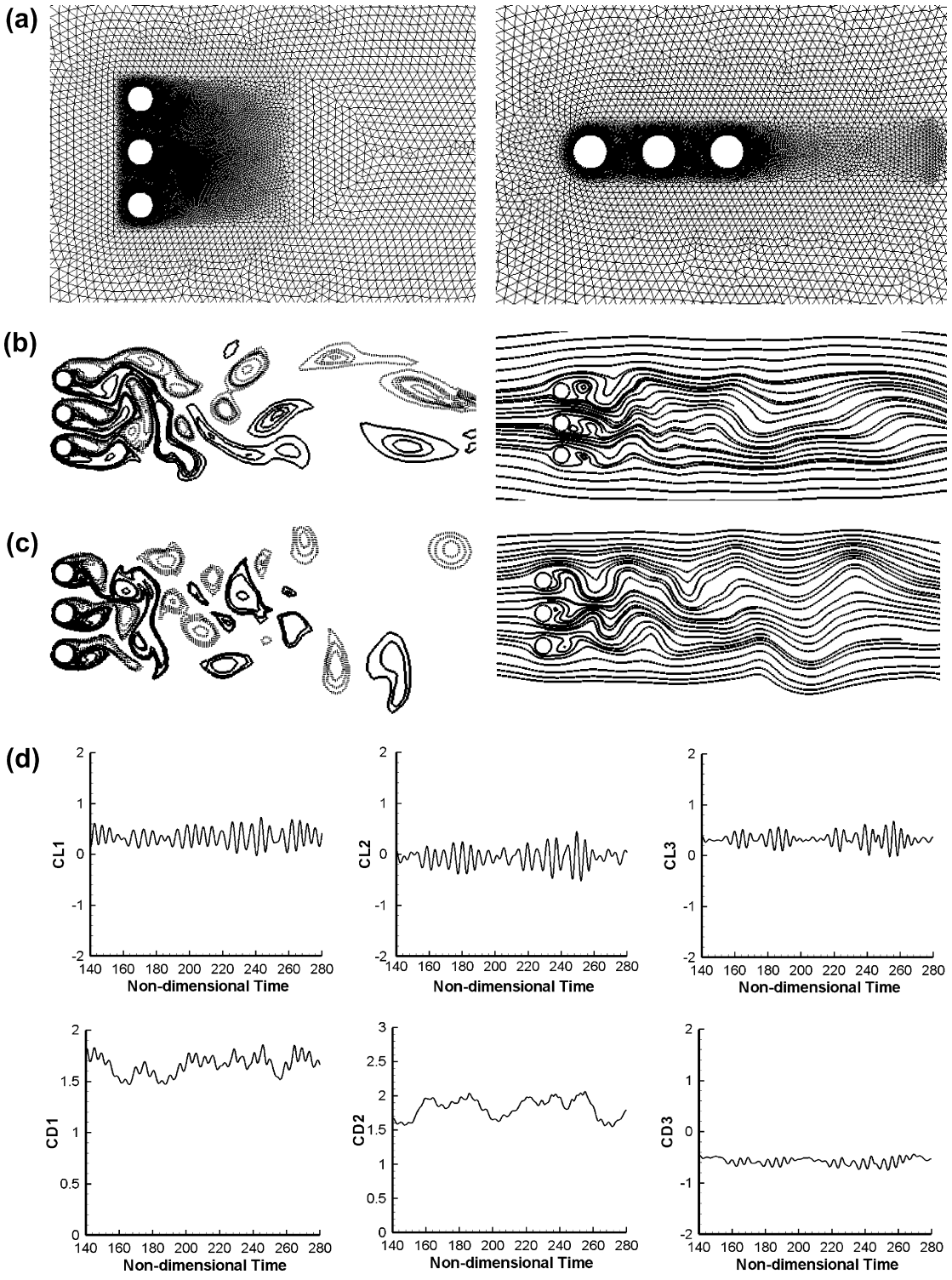

Fig. 6. (a) Close-up view of the triangular mesh around three circular cylinders (T = 2D and L = 2D), (b) Vorticity contours and streamlines of flow past three side-by-side circular cylinders (T = 2D) at Re = 100, (c) Vorticity contours and streamlines of flow past three side-by-side circular cylinders (T = 2D) at Re = 200, (d) Lift and drag coefficients of flow past three circular cylinders (T = 2D) at Re = 100, (e) Lift and drag coefficients of flow past three side-by-side circular cylinders (T = 2D) at Re = 200.

nomena result in a narrow wake pattern behind the upper cylinder as compared to the lower one. Due to this bifurcation of flip-flopping and deflected wake pattern in the downstream region, the drag coefficient of central cylinder is marginally higher than that of upper cylinder but the lower cylinder experiences substantially lower value of drag coefficient which will increase with the increase in gap spacing between the cylinders. The results for the three cylinders in side-by-side arrangement are indicated by associating a number along with CL and CD. '1' stands for the upper cylinder, '2' stands for the middle cylinder and '3' stands for the lower cylinder.

Fig. 7a and b presents the vorticity contours and streamlines of flow past three cylinders in tandem for L = 2D at Re = 100 and 200 respectively at instantaneous non-dimensional time t = 250. It is observed that at Re = 100 the flow maintains a steady state though the Reynolds number is much greater than the critical value for

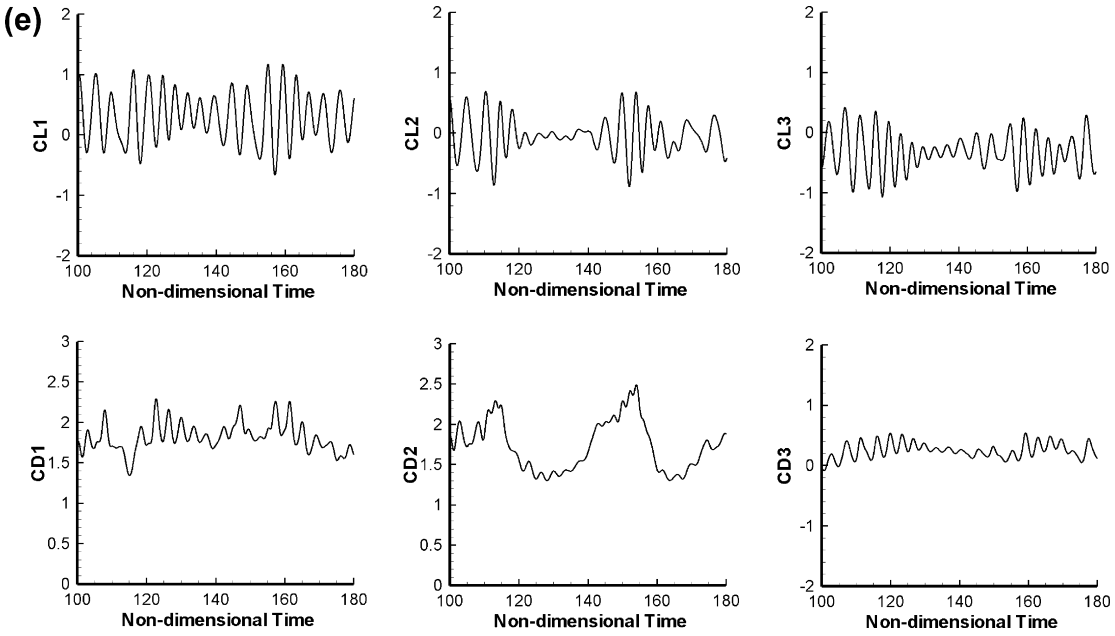

Fig. 6 (*continued*)

single cylinder (Re ≈ 49). From the streamline plots for Re = 100, it is observed that the flow in the gap region between the cylinders is rather restricted. Also, the shear layer which is separated from the inside surface of the upstream cylinder reattaches onto the outer surface of the middle cylinder. The same phenomenon also occurs between middle cylinder and downstream cylinder. This flow regime has been classified by Zdravkovich (1977) as the steady reattachment. Fig. 7c and d shows the temporal histories of drag and lift coefficients for flow past three tandem cylinders at Re = 100 and 200 respectively. From Fig. 7c, it can be observed that amplitude of lift coefficient remains almost equal to zero even after sufficient numbers of time-steps. It implies that the unsteady behaviour initially produced by the artificial numerical perturbation due to round off errors, etc. is gradually dissipated by viscosity. However with increase in Reynolds number (Re = 200), the flow field between the cylinders (upstream-middle and middle-downstream) becomes marginally unsteady. Flow behind the downstream cylinder becomes unsteady and a sparse Karman vortex street is formed. This gap (L = 2D) falls in the critical gap regime as proposed by Zdravkovich (1977) and therefore the streamline and vorticity contours and the temporal behaviour of lift and drag coefficients for Re = 200 case is as per expectation. The results for the three cylinders in tandem arrangement are indicated by associating a number along with CL and CD. '1' stands for the upstream cylinder, '2' stands for the middle cylinder and '3' stands for the downstream cylinder.

Table 6 mentions the mean value and amplitude of drag and lift coefficients for three cylinders at Re = 100 and 200 for side-by-side and tandem arrangements. It is observed that for side-by-side arrangements, the mean values of drag coefficient for the upper cylinder and central cylinders are comparable with later being marginally higher than the former. But the lower cylinder experiences very low drag coefficients due to the bifurcation of the wake pattern in the downstream. However, for cylinders in tandem arrangement, the upstream cylinder experiences higher drag than the other two cylinders. The drag coefficient for the downstream cylinder is very low as compared to the other upstream cylinders due to the sparse Karman vortex street behind it. The negative value of drag coefficients obtained in the present calculations for lower cylinder in side-by-side arrangement and for downstream cylinder in tandem arrangement agrees well with the results of Meneghini et al. (2001) who proposed that this will change to positive value once the separation gap increases beyond three times the diameter of the cylinders. However, the Strouhal number values are not obtainable for the cylinders with lower transverse gap (T = 2D) from our results. With flip-flopping wake pattern at such a low transverse gap, FFT of the lift coefficient does not produce any distinct dominant frequency. For cylinders in tandem arrangement, the steady wake pattern obtained at Re = 100 has no vortex shedding frequency. At Re = 200, due to flip-flopping nature of wake patterns, any distinct dominant frequency is not obtained from the FFT analysis of the lift coefficient. Therefore no shedding frequency is mentioned for three cylinders in tandem arrangement at such a low longitudinal gap between the cylinders.

8.3.2. Case II: side-by-side (T = 5D) and tandem (L = 5D) arrangement

Due to irregularities in the flow patterns in either of the arrangements (side-by-side or tandem) of three cylinders with T = 2D and L = 2D, it has been a difficult task to conclude on the nature of the flow behind the cylinders with such low separation gaps which lie within critical gap region. In order to obtain a distinct flow pattern behind the cylinders, numerical simulations were subsequently performed for the case of T = 5D and L = 5D for side-by-side and tandem arrangement of three circular cylinders respectively. Distribution of cells in the complete domain is shown in Fig. 8. The transverse distance between the central cylinder and the outer boundary is kept fixed which would produce comparable transverse blockage ratio so that it will not have much effect on the flow. Close-up views of the triangular mesh around three circular cylinders for the two cases are shown in Fig. 9a. In both the cases, the non-dimensional time step used is 0.0005. In the present study, the unsteady flow at Re = 100 and 200 are simulated on a triangular mesh with 21,558 cells and 11,015 nodes for T = 5D case and with 25,180 cells and 12,840 nodes for L = 5D case respectively.

Fig. 9b and c presents the vorticity contours and streamlines of flow past three side-by-side cylinders for T = 5D at Re = 100 and 200 respectively at instantaneous non-dimensional time t = 220. It is observed that with larger transverse gap (5D) which is well beyond the critical gap, three synchronized Karman vortex streets are

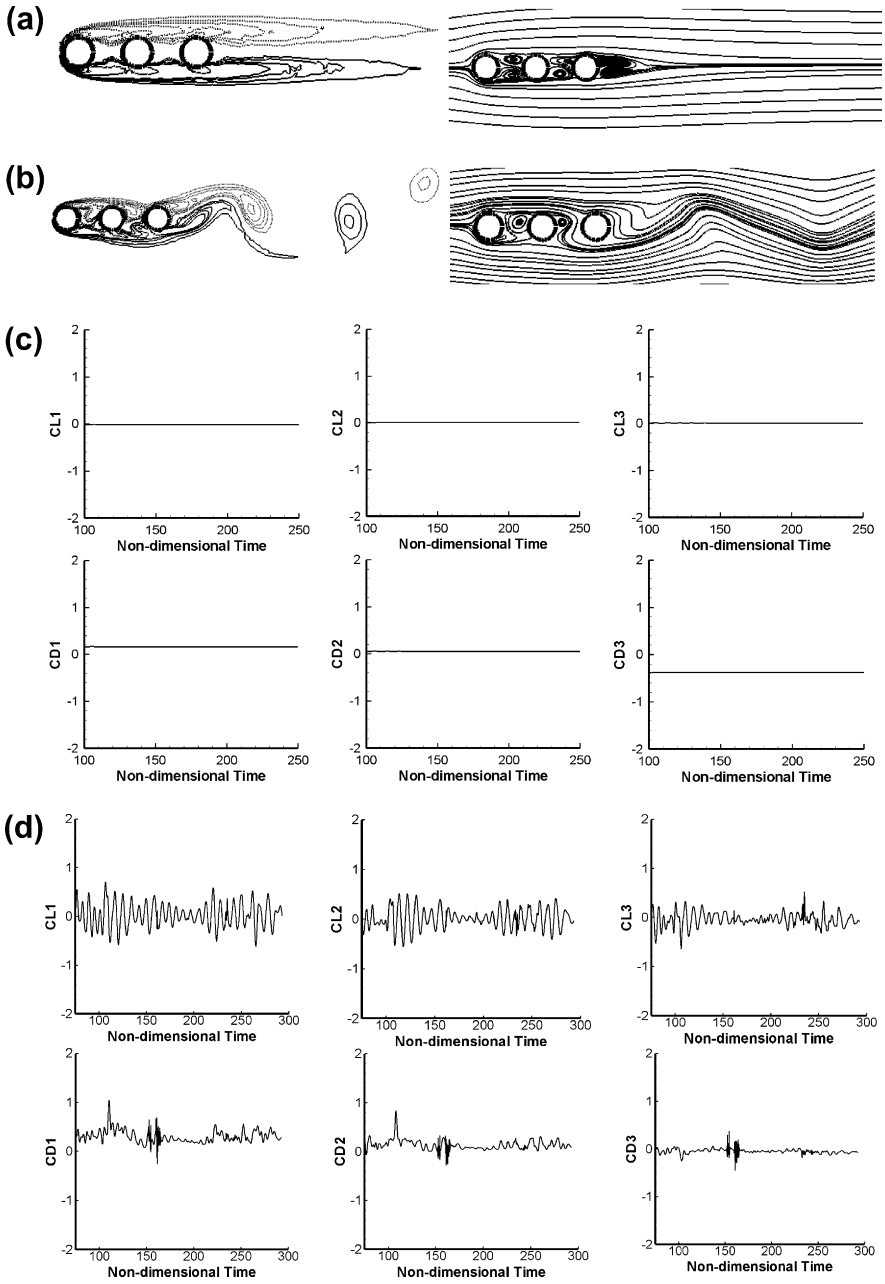

Fig. 7. (a) Vorticity contours and streamlines of flow past three circular cylinders in tandem (L = 2D) at Re = 100, (b) Vorticity contours and streamlines of flow past three circular cylinders in tandem (L = 2D) at Re = 200, (c) Lift and drag coefficients of flow past three circular cylinders (L = 2D) at Re = 100, (d) Lift and drag coefficients of flow past three circular cylinders in tandem (L = 2D) at Re = 200.

Table 6
Values of flow parameters for flow field around three circular cylinders at Re = 100 and 200 for side-by-side and tandem arrangement.

Parameters		Drag coefficient (CD)		Lift coefficient (CL)	
Reynolds number		Re = 100	Re = 200	Re = 100	Re = 200
T = 2D	Upper Cylinder	1.72	1.91	0.35 ± 0.3	0.4 ± 0.6
	Middle Cylinder	1.86	2.05	0.0 ± 0.4	0.0 ± 0.55
	Lower Cylinder	−0.58	0.32	0.35 ± 0.3	−0.4 ± 0.5
L = 2D	Upstream Cylinder	0.2	0.32	0.0	0.0 ± 0.5
	Middle Cylinder	0.08	0.13	0.0	0.0 ± 0.4
	Downstream Cylinder	−0.4	−0.05	0.0	−0.1 ± 0.22

formed behind the three cylinders. Fig. 9d and e shows the temporal histories of drag and lift coefficients. The synchronized variation of lift and drag coefficients with time also ensures fully periodic flow with synchronized vortex shedding from the cylinders. It is also observed that modulation occurs and the observed modulation period is very large as compared to the vortex shedding peri-

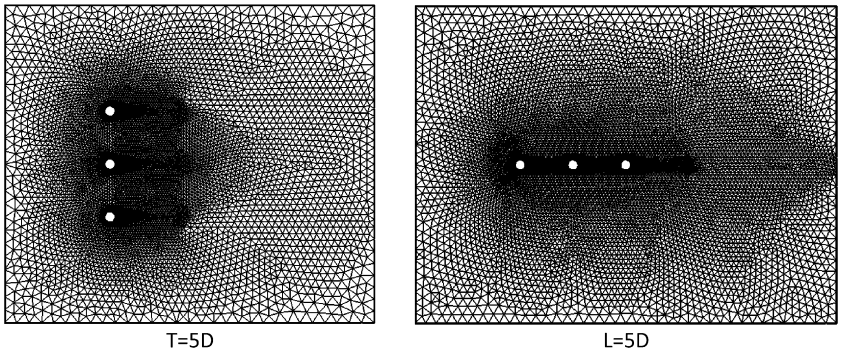

Fig. 8. Complete flow domain with three circular cylinders in side-by-side (T = 5D) and tandem (L = 5D) arrangement.

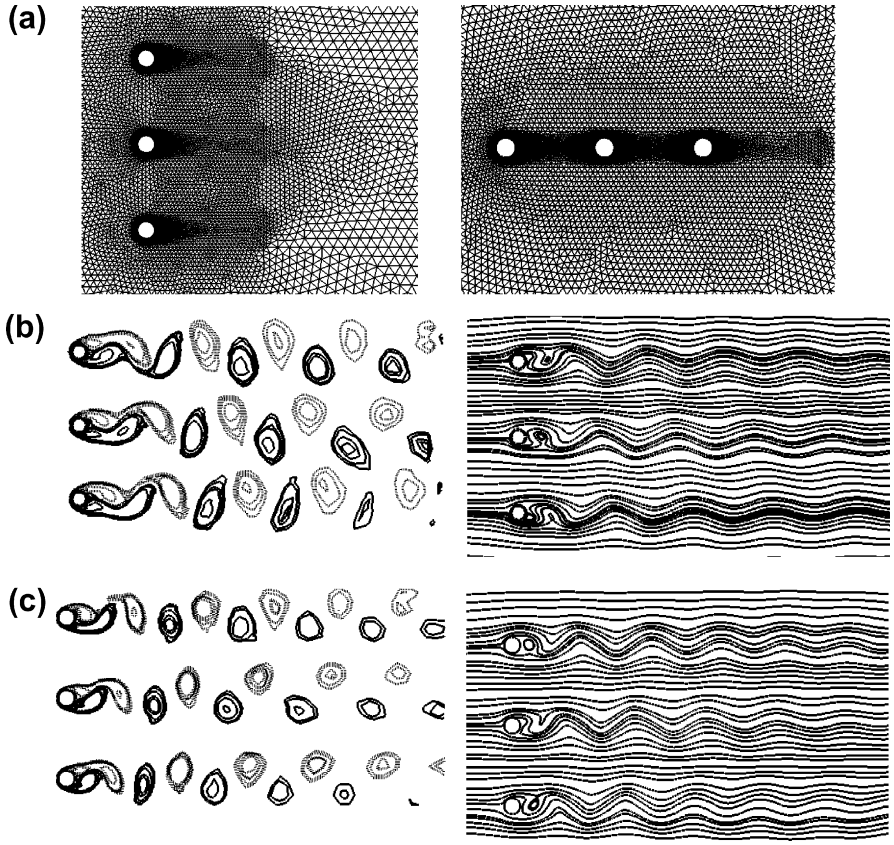

Fig. 9. (a) Close-up view of the triangular mesh around three circular cylinders (T = 5D and L = 5D), (b) Vorticity contours and streamlines of flow past three side-by-side circular cylinders (T = 5D) at Re = 100, (c) Vorticity contours and streamlines of flow past three side-by-side circular cylinders (T = 5D) at Re = 200, (d) Lift and drag coefficients of flow past three side-by-side circular cylinders (T = 5D) at Re = 100, (e) Lift and drag coefficients of flow past three side-by-side circular cylinders (T = 5D) at Re = 200.

od. This observation was also highlighted by Kang (2004) in his numerical simulation for similar flow configuration. According to the FFT analyses, the three cylinders shed their vortices with frequencies close to the single cylinder case both at Re = 100 and 200 but the shedding frequency for the two outer cylinders is slightly smaller than that for the central one. This marginal difference between the two vortex shedding frequencies obviously causes the modulation phenomena with a very low modulation frequency. Thus due to the modulation characteristics, the flow structure is called modulation synchronized flow pattern. Sumner et al. (1999) has reported synchronized-unbiased vortex shedding at similar gap spacing range (T > 3D) in the turbulent regime. Thus, it is evident that the modulation phenomena in the present case may be due to the lower Reynolds numbers used for the flow calculations. It is also observed that the mean value of lift coefficient is positive for upper cylinder, zero for middle cylinder and negative for lower cylinder. Also, it is observed that the flow parameters tend towards those for single cylinder for 5D transverse gap. This is due to the decreased flow interference as the transverse gap between the cylinders further increases.

Fig. 10a and b presents the vorticity contours and streamlines of flow past three circular cylinders in tandem for T = 5D at Re = 100 and 200 respectively at instantaneous non-dimensional time t = 220. When the longitudinal gap between the cylinders is increased to 5D, the flow pattern in the gap region experiences a distinct change. The phenomenon involving the separation and reattachment of shear layer from the upstream cylinder to the immediate downstream cylinder is no more prevalent for the pres-

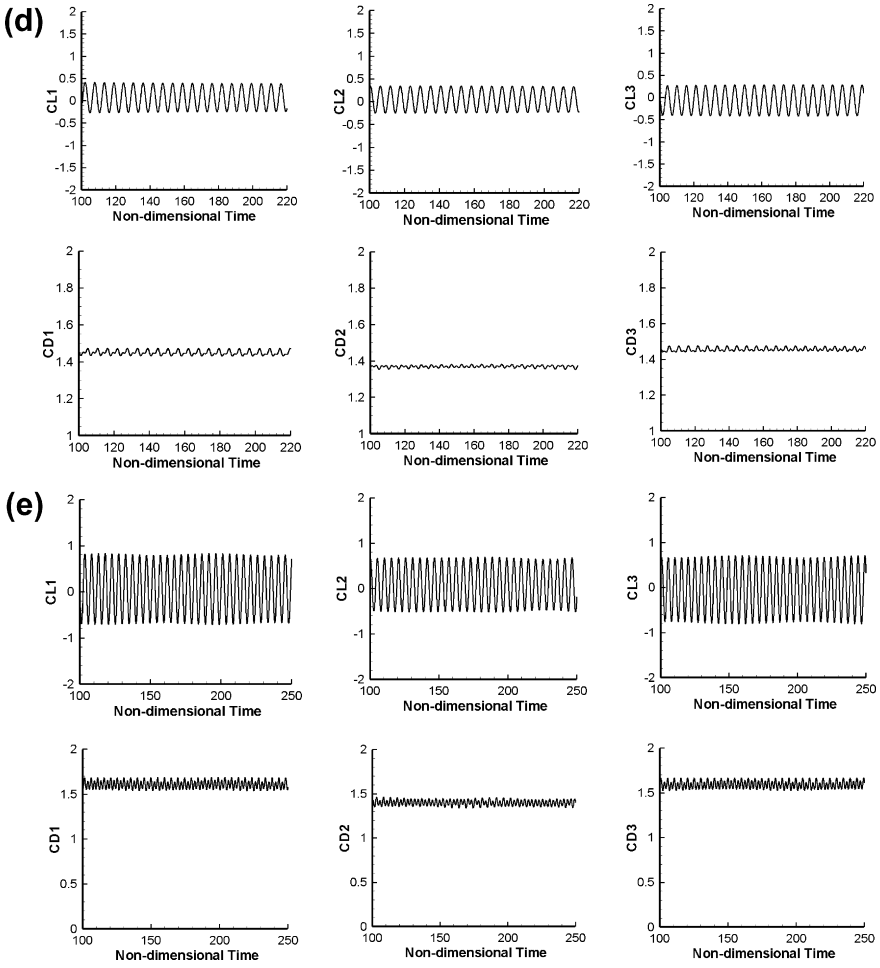

Fig. 9 (*continued*)

ent case. Instead, Karman vortex streets are observed between the cylinders. From the vorticity contours, it is observed that the vortex shedding from the downstream cylinder is highly disturbed by the impingement of the vortex streets emerging from upstream and middle cylinders. The temporal histories of lift and drag coefficients are shown in Fig. 10c and d. It can be seen that the synchronization occurs between the impingement flow and vortex shedding from the downstream cylinder.

The mean value and the amplitude of drag and lift coefficients and the Strouhal number of the present numerical results are listed in Table 7. The results of flow past single circular cylinder are also included in this table for comparison. It can be seen that when the gap between the cylinders is increased to $L = 5D$, the flow parameters of upstream cylinder become closer to those of a single cylinder. But for the downstream cylinder, the solution difference with a single cylinder confirms the influence of flow impingement on the flow field. It is observed that the Strouhal number value remains same for all the cylinders at a particular Reynolds number in either of the arrangements. This phenomenon agrees well with the results of Liang et al. (2009).

9. Conclusions

A numerical method has been proposed to solve two dimensional Navier–Stokes equations for incompressible viscous flows. The solver is based on a cell-centered finite-volume scheme for unstructured triangular meshes. The algorithm has been used to study the interference effect of vortices in the laminar flows involving three cylinders in tandem and side-by-side arrangements at Re = 100 and 200. The algorithm is first validated for laminar flow past a single cylinder and two cylinders in side-by-side arrangements at different transverse gaps between the cylinders. The results show good qualitative agreement with the computational results from other researchers. The present scheme demonstrates good convergence characteristics and reasonably good accuracy as is evident from comparison of results with available literature. The present CFRUNS solver can be considered to be as good as other reported unstructured grid solvers. In the present study, the flow was assumed to be two-dimensional and laminar in all possible arrangement of cylinders. Due to the augmented characteristic length when the cylinders were in close proximity, three-dimensional phenomena might emerge over the ranges of relatively higher Reynolds number and small gap spacings.

For the case of flows past three cylinders in tandem, it is observed that the downstream cylinder which lies in the wake of the upper cylinder experiences very large unsteady forces that can give rise to wake-induced flutter. This phenomenon is more likely to occur with less longitudinal gap between the cylinders. With relatively lower longitudinal gap ($L = 2D$), steady wake pattern was obtained at Re = 100 but sparse Karman street was observed at Re = 200. In this case, any distinct dominant shedding frequencies were not reported by the FFT analyses of the lift coefficients. When the longitudinal gap is increased ($L = 5D$), there were no flow separation or reattachment of shear layer from the

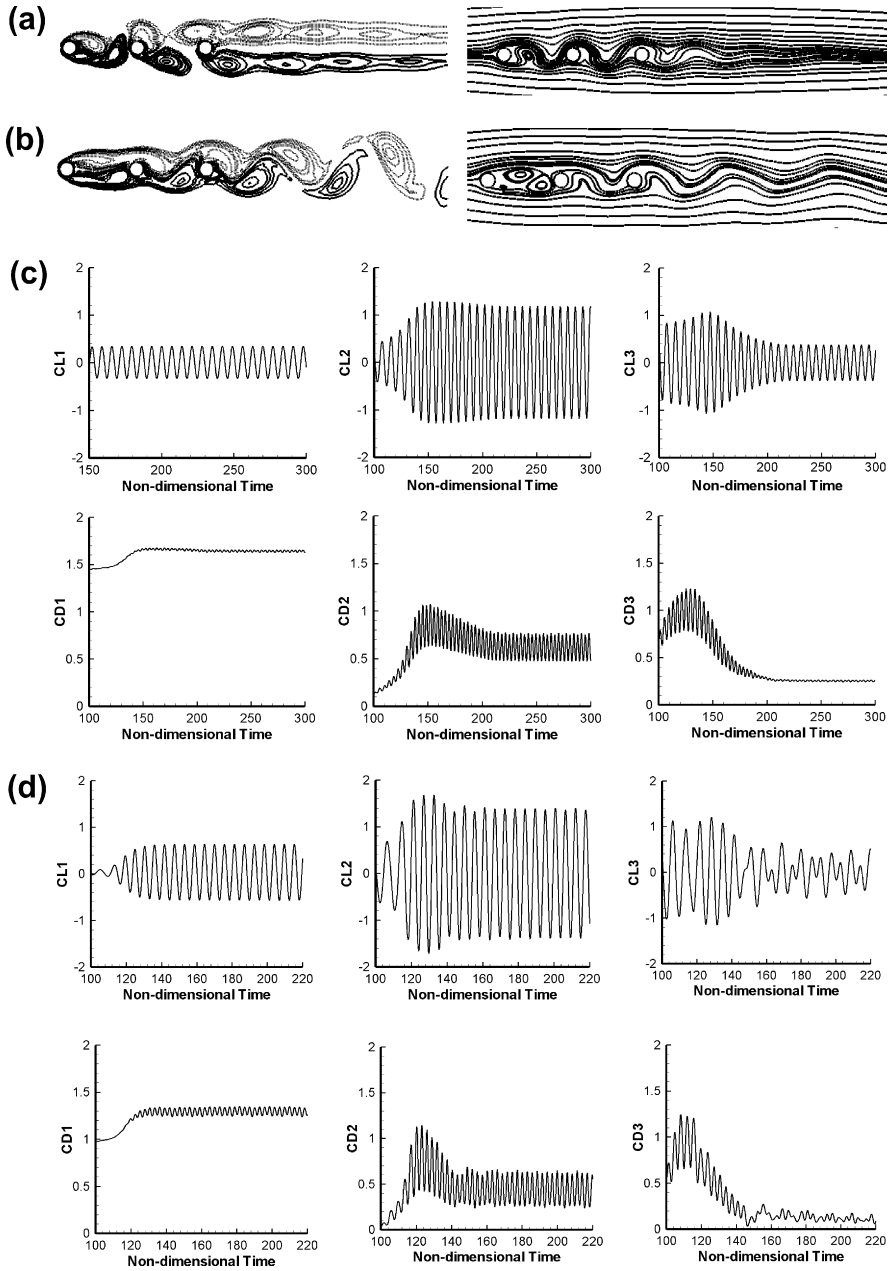

Fig. 10. (a) Vorticity contours and streamlines of flow past three circular cylinders in tandem (L = 5D) at Re = 100, (b) Vorticity contours and streamlines of flow past three circular cylinders in tandem (L = 5D) at Re = 200, (c) Lift and drag coefficients of flow past three circular cylinders in tandem (L = 5D) at Re = 100, (d) Lift and drag coefficients of flow past three circular cylinders in tandem (L = 5D) at Re = 200.

Table 7
Values of flow parameters for flow field around three circular cylinders at Re = 100 and 200 for side-by-side and tandem arrangement.

Parameters		Drag coefficient (CD)		Lift coefficient (CL)		Strouhal number (St)	
Reynolds number		Re = 100	Re = 200	Re = 100	Re = 200	Re = 100	Re = 200
Single Circular cylinder		1.352 ± 0.01	1.32 ± 0.05	0.0 ± 0.278	0.0 ± 0.602	0.161	0.192
T = 5D	Upper Cylinder	1.45 ± 0.02	1.61 ± 0.07	0.0 ± 0.35	0.0 ± 0.78	0.1766	0.1922
	Middle Cylinder	1.36 ± 0.01	1.40 ± 0.05	0.0 ± 0.32	0.0 ± 0.66	0.1796	0.2019
	Lower Cylinder	1.45 ± 0.02	1.60 ± 0.07	0.0 ± 0.35	0.0 ± 0.73	0.1766	0.1922
L = 5D	Upstream Cylinder	1.64 ± 0.02	1.29 ± 0.05	0.0 ± 0.35	0.0 ± 0.6	0.1452	0.1766
	Middle Cylinder	0.62 ± 0.5	0.46 ± 0.165	0.0 ± 1.21	0.0 ± 1.37	0.1452	0.1766
	Downstream Cylinder	0.25 ± 0.008	0.12 ± 0.044	0.0 ± 0.39	0.0 ± 0.45	0.1452	0.1766

upstream cylinder to the immediate downstream cylinder. Instead, Karman vortex streets were observed between the cylinders. However, the vortex shedding from the downstream cylinder was highly disturbed by the impingement of the upstream vortex streets emerging from upstream and middle cylinders. The vortex shedding frequency strongly depended on the gap spacing. The

FFT analyses of the lift coefficients show distinct identical vortex shedding frequencies for all the cylinders.

For the case of flows past two and three cylinders in side-by-side arrangement at less transverse gap between the cylinders, it was observed that the complex vortex interactions are intense in the near wake region. Depending on the gap spacings, different wake patterns like in-phase or anti-phase synchronized wake patterns (two-cylinders with $T = 3D$), deflected wake patterns (two-cylinders with $T = 1.5D$), modulated synchronized wake patterns (three-cylinders with $T = 5D$) and bifurcated parallel flip-flopping wake patterns (three-cylinders with $T = 2D$) were observed.

It has been found in general that flows involving two and three cylinders show a strong dependence on the Reynolds number as well as gap spacings between the cylinders with the later playing a dominant role as compared with the flows past a single cylinder. Similar to the flow past a single circular cylinder, in case of flows past two- and three-cylinder arrays, the Strouhal number tends to increase as Reynolds number increases which implies that there is a more rapid vortex shedding. It is observed that the interference effect of cylinders due to increase in Reynolds number is more sensitive in case of tandem arrangement as compared to side-by-side arrangement. In tandem arrangement of cylinders, the flow field behind the downstream cylinder develops from steady state into an unsteady state as Reynolds number increases. It has also been observed that in case of multi-cylinder arrangement, the Strouhal number values for each cylinder remain same for all the cylinders at a particular Reynolds number. In general, the vortex shedding frequencies for tandem cylinders were found to be lower than the side-by-side cylinders.

Acknowledgements

This work is partially supported by the Air Force Office of Scientific Research, AFRL, USAF, through AOARD Grant Nos. FA2386-08-1-4088 and FA2386-09-1-4109 and by Aeronautics R&D Board, Ministry of Defence, Government of India research grant, Sanction letter No. DARO/08/1031445/M/I, dated 16.04.2008.

References

Abdallah, S., 1987a. Numerical solution for the pressure Poisson equation with Neumann boundary condition using a non staggered grid, I. Journal of Computational Physics 70, 182–192.

Abdallah, S., 1987b. Numerical solution for the pressure Poisson equation with Neumann boundary condition using a non staggered grid, II. Journal of Computational Physics 70, 193–202.

Bearmann, P.W., Wadcock, A.J., 1973. The interaction between a pair of circular cylinders normal to a stream. Journal of Fluid Mechanics 61, 499–511.

Braza, M., Chassaing, P., Ha Minh, H., 1986. Numerical study and physical analysis of the pressure and velocity fields in the near wake of a circular cylinder. Journal of Fluid Mechanics 163, 79–130.

Chang, K.S., Song, C.J., 1990. Interactive vortex shedding from a pair of circular cylinders in a transverse arrangement. International Journal for Numerical Methods in Fluids 11, 317–329.

Choi, Seok Ki, Nam, Ho Yun, Cho, Mann, 1993. Use of the momentum interpolation method for numerical solution of incompressible flows in complex geometries: choosing cell face velocities. Numerical Heat Transfer Part B 23, 21–41.

Deng, G.B., Piquet, J., Queutey, P., Visonneau, M., 1994. Incompressible flow calculations with a consistent physical interpolation – finite volume approach. Computers and Fluids 23 (8), 1029–1047.

Ding, H., Shu, C., Yeo, K.S., Xu, D., 2007. Numerical simulation of flows around two circular cylinders by mesh-free least square-based finite difference methods. International Journal for Numerical Methods in Fluids 53, 305–332.

Farrant, T., Tan, M., Price, W.G., 2001. A cell boundary element method applied to laminar vortex shedding from circular cylinders. Computers and Fluids 30, 211–236.

Friehe, C.A., 1980. Vortex shedding from cylinders at low Reynolds numbers. Journal of Fluid Mechanics 100, 237–241.

Gresho, P.M., Chan, S.T., Lee, R.L., Upson, C.D., 1980. On the Time Dependent Solution of the Incompressible Navier–Stokes Equations. Recent Advances in Numerical Methods in Fluids. Pineridge Press, Swansea.

Jester, W., Kallinderis, Y., 2003. Numerical study of incompressible flow about fixed cylinder pairs. Journal of Fluids and Structures 17, 561–577.

Kang, S., 2003. Characteristics of flow over two circular cylinders in a side–side arrangement at low Reynolds numbers. Physics of Fluids 15 (9), 2486–2498.

Kang, S., 2004. Numerical study on laminar flow over three side-by-side cylinders. KSME International Journal 18 (18), 1869–1879.

Liu, Kun, Ma, Dong-Jun, Sun, De-Jun, Yin, Xie-Yuan, 2007. Wake patterns of flow past a pair of circular cylinders in side-by-side arrangements at low Rynolds numbers. Journal of Hydrodynamics 19 (6), 690–697.

Liang, C., Papadakis, G., Luo, X., 2009. Effect of tube spacing on the vortex shedding characteristics of laminar flow past an inline tube array: a numerical study. Computers and Fluids 38, 950–964.

Meneghini, J.R., Saltara, F., Siqueira, C.L.R., Ferrari Jr, J.A., 2001. Numerical simulation of flow interference between two circular cylinders in tandem and side-by-side arrangement. Journal of Fluids and Structures 15, 327–350.

Mittal, S., Kumar, V., Raghuvanshi, A., 1997. Unsteady incompressible flows past two cylinders in tandem and staggered arrangement. International Journal for Numerical Methods in Fluids 25, 1315–1344.

Mizusima, J., Ino, Y., 2008. Stability of flows past a pair of circular cylinders in a side-by-side arrangement. Journal of Fluid Mechanics 595, 491–507.

Rhie, C.M., Chow, W.L., 1983. Numerical study of turbulent flow past an airfoil with trailing edge separation. AIAA Journal 21 (11).

Roshko, A., 1954. On the Drag and Shedding Frequency of Two Dimensional Bluff Bodies. NACA TN, pp. 3169.

Roy, A., Bandyopadhyay, G., 2006. A finite volume method for viscous incompressible flows using a consistent flux reconstruction scheme. International Journal for Numerical Methods in Fluids 52, 297–319.

Silva, A.L.F. de Lima, Silva, A.R., Neto, A.S., 2007. Numerical simulation of two-dimensional complex flows around bluff bodies using the immersed boundary method. Journal of the Brazilian Society of Mechanical Science and Engineering 3 (4), 379–387.

Slaouti, A., Stansby, P.K., 1992. Flow around two circular cylinders by the random-vortex method. Journal of Fluids and Structures 6, 641–670.

Stansby, P.K., Slaouti, A., 1981. A numerical study of vortex shedding from one and two cylinders. Aeronautical Quarterly 32, 48–71.

Sumner, D., Wong, S.S.T., Price, S.J., Paidoussis, M.P., 1999. Fluid behavior of side-by-side circular cylinders in steady cross-flow. Journal of Fluids and Structures 13, 309–338.

Tritton, D.J., 1959. Experiments on the flow past a circular cylinder at low Reynolds numbers. Journal of Fluid Mechanics 6, 547.

Wiesenberger, V.C., 1921. Neuere festellungen über die Gesetze des üssigkeits und Luftwiderstands. Physik. Z. 22, 231.

Williamson, C.H.K., 1985. Evolution of a single wake behind a pair of bluff bodies. Journal of Fluid Mechanics 159, 1–18.

Xu, S.J., Zhou, Y., So, R.M.C., 2003. Reynolds number effects on flow structure behind two side-by-side cylinders. Physics of Fluids 15 (5), 1214–1219.

Zdravkovich, M.M., 1977. Review of flow interference between two circular cylinders in various arrangements. Journal of Fluids Engineering (ASME) 99, 618–633.

Zhang, H.J., Zhou, Y., 2001. Effect of unequal spacing on vortex streets behind three side-by-side cylinders. Physics of Fluids 13, 3675–3686.

Zhou, Y., So, R.M.C., Liu, M.H., Zhang, H.J., 2000. Complex turbulent wakes generated by two and three side-by-side cylinders. International Journal of Heat and Fluid Flow 21, 125–133.